Production of forward heavy-flavor dijets at the LHCb within the k_T-factorization approach

Rafał Maciuła,[1,*] Roman Pasechnik,[2,†] and Antoni Szczurek[1,3,‡]

[1]*Institute of Nuclear Physics, Polish Academy of Sciences, ul. Radzikowskiego 152, PL-31-342 Kraków, Poland*

[2]*Department of Astronomy and Theoretical Physics, Lund University, SE-223 62 Lund, Sweden*

[3]*College of Natural Sciences, Institute of Physics, University of Rzeszów, ul. Pigonia 1, PL-35-310 Rzeszów, Poland*

(Received 23 February 2022; accepted 19 August 2022; published 15 September 2022)

We calculate differential cross sections for $c\bar{c}$- and $b\bar{b}$-dijet production in pp scattering at $\sqrt{s} = 13$ TeV in the k_T-factorization and hybrid approaches with different unintegrated parton distribution functions (uPDFs). We present distributions in the transverse momentum and pseudorapidity of the leading jet, the rapidity difference between the jets and the dijet invariant mass. Our results are compared to recent LHCb data on forward production of heavy-flavor dijets, measured recently for the first time individually for both charm and bottom flavors. We find that an agreement between the predictions and the data within the full k_T factorization is strongly related to the modeling of the large-x behavior of the gluon uPDFs, which is usually not well constrained. The problem may be avoided following the hybrid-factorization approach. Then, we obtain a good description of the measured distributions with the parton-branching, Kimber-Martin-Ryskin, Kutak-Sapeta, and Jung setA0 models for the gluon uPDF. We also calculate differential distributions for the ratio of the $c\bar{c}$ and $b\bar{b}$ cross sections. In all cases we obtain a ratio close to 1, which is caused by the condition on the minimal jet transverse momentum ($p_T^{\rm jet} > 20$ GeV) introduced in the experiment, that makes the role of the heavy-quark mass almost negligible. The LHCb experimental ratio seems a bit larger than the theoretical predictions. We discuss potentially important for the ratio effect of c- or b-quark gluon radiative corrections related to emission outside of the jet cone. The found effect seems rather small. A more refined calculation requires full simulation of c and b jets, which goes beyond of the scope of this paper.

DOI: 10.1103/PhysRevD.106.054018

I. INTRODUCTION

The production of heavy flavors is a laboratory for studying the effects of perturbative QCD. It is very often used to "extract" parton distribution functions (PDFs) for gluons in the nucleon. This is usually done within the collinear-factorization approximation. There are a few methods to experimentally investigate charm- and bottom-quark production at hadron colliders. One is the direct procedure based on a full reconstruction of all decay products of open D and B mesons. The corresponding hadronic decay products can be used to build invariant-mass distributions, permitting the direct observation of D or B mesons as a peak in the experimental invariant-mass spectra. Different charm mesons ($D^{\pm}$, $D^0/\bar{D}^0$, or $D_s^{\pm}$) have been used in this context at the LHC, including ALICE, ATLAS, and CMS measurements at midrapidities [1–6] and the LHCb measurements in forward directions [7,8]. Similarly B^0 and $B^{\pm}$ mesons were studied with ATLAS and CMS [9–11].

Studies of open heavy-flavor mesons require some additional modeling that takes into account effects related to a transition from quarks to hadrons. The transition is called hadronization or parton fragmentation and can be so far dealt only with phenomenological models. In principle, in the case of multiparticle final states the Lund string model [12] and the cluster fragmentation model [13] are often used; however, these methods were originally devoted to midrapidities and their application in forward directions is an open question. The hadronization of heavy quarks in non–Monte Carlo calculations is usually done with the help of fragmentation functions. The latter are similar to PDFs and provide the probability of finding a hadron produced

*rafal.maciula@ifj.edu.pl
†roman.pasechnik@thep.lu.se
‡antoni.szczurek@ifj.edu.pl

from a high-energy quark or gluon. Unfortunately, in this case the fragmentation-function technique also leads to some ambiguities [14,15], especially in forward directions.

Inclusive open heavy-flavor meson production at the LHC was studied differentially in both collinear [16–20] and k_T-factorization approaches [21–27] as well as in the dipole model [19,28]. The inclusive distributions describe the experimental ones within theoretical uncertainties (i.e., the chosen heavy-quark mass, renormalization and factorization scales, and parton distributions). Correlation measurements (meson-antimeson or meson-meson pairs) were also performed by the LHCb [29] and CMS [30] collaborations. Those data were nicely explained in the framework of the k_T-factorization approach [21,25,26,31,32]. Similar studies were also performed with the next-to-leading-order (NLO) collinear factorization [33], but some problems with the description of the data were identified that can only be solved by introducing a phenomenological intrinsic transverse momentum or by matching parton-level calculations and parton showers [34]. In any case, theoretical calculations of open heavy-flavor meson production are to some extent to some extent limited by not fully understood fragmentation.

Another method is to measure heavy-quark/-antiquark jets. The reconstruction of jets containing heavy-flavor hadrons provides more direct access to the primary heavy-flavor parton kinematics than an inclusive measurement of heavy-flavor hadrons and allows to study production and fragmentation effects separately. In the LHC era this is used almost routinely for b or $\bar{b}$ jets. Corresponding measurements were performed by the ATLAS [35], CMS [36], and (very recently) ALICE [37] collaborations. The ALICE experiment can reconstruct the b-flavored jets down to extremely low transverse momenta, such as $p_T \approx 10$ GeV [37]. The CMS collaboration recently measured jet shapes for b jets in pp collisions for the first time [38]. Also, $b\bar{b}$ dijets were measured by the ATLAS [39] and CMS [40] experiments.

Although b-jet identification algorithms have been deployed for several decades, the task of identifying c jets is more challenging [41]. Some first trials for inclusive c-jet studies were initiated by the CMS [42], ALICE [43], and LHCb [44] collaborations. Very recently, the LHCb Collaboration identified charm jets in Run 2 [45]. Last year, the LHCb Collaboration reported very unique results for the simultaneous measurement of $c\bar{c}$ and $b\bar{b}$ dijets in pp scattering at 13 TeV [46]. This was the first $c\bar{c}$-dijet differential cross-section measurement at the hadron collider.

Here we wish to explore the new LHCb data for $c\bar{c}$- and $b\bar{b}$-dijet production within the k_T-factorization approach. This data set is extremely interesting from the point of view of constraining unintegrated gluon densities in the proton. The data points were obtained for $2.2 < \eta_{\mathrm{jet1,2}} < 4.2$, $p_T^{\mathrm{jet1,2}} > 20$ GeV, jet radius $R_{\mathrm{cone}} = 0.5$, and the difference in the azimuthal angle between the jets $\Delta\varphi > 1.5$. The specific kinematics set and characteristic mechanisms behind the considered reactions have many benefits in phenomenological applications. In principle, because of the large scales involved, the perturbative QCD (pQCD) methods are fully applicable and almost no heavy-quark mass effects are expected. There is no need to use fragmentation functions and the production mechanism is fully dominated by gluon interactions. In addition, as will be discussed in the following, the forward direction explored in the LHCb measurement allows for a direct probe of different models of the unintegrated parton distribution functions (uPDFs) for the gluon, simultaneously in both small- and large-x regions. All of these aspects make the study very interesting in the context of present and future collider experiments on forward heavy-flavor production, including those recently proposed by the Forward Physics Facility community [47]. It might also be of great importance in understanding the dynamics behind mechanisms of prompt atmospheric neutrino flux at present IceCube, Baikal-GVD, or other future neutrino observatories.

II. DETAILS OF THE MODEL CALCULATIONS

A. k_T-factorization framework

We recall the theoretical formalism for the calculation of inclusive $Q\bar{Q}$-pair production in the k_T-factorization approach [48], where $Q = c$, b stands for the charm and beauty quarks, respectively. In this framework the transverse momenta k_t (virtualities) of both partons entering the hard process are taken into account, in both the matrix elements and the parton distribution functions. Emission of the off-mass-shell initial-state partons is encoded in the transverse-momentum-dependent (unintegrated) parton distribution functions. In the case of heavy-flavored dijet production, the parton-level cross section is usually calculated via the leading-order (LO) $g^*g^* \to Q\bar{Q}$ fusion mechanism of off-shell initial-state gluons, which is the dominant

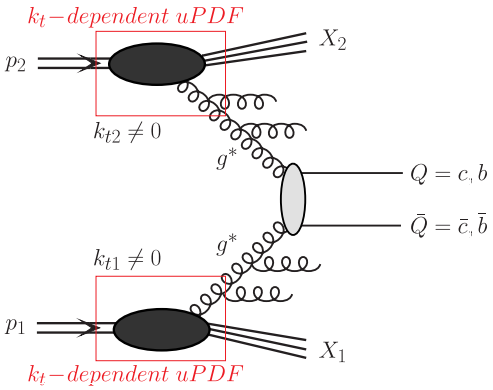

FIG. 1. Diagrammatic representation of the leading-order mechanism of heavy-flavored dijet production in the k_T-factorization approach.

process at high energies. As we will show when presenting our numerical results, the $q^*\bar{q}^* \to Q\bar{Q}$ mechanism remains subleading in the whole kinematical domain considered here. Then, the hadron-level differential cross section for $Q\bar{Q}$-dijet production (see the diagram in Fig. 1), formally at leading order, reads

$$\frac{d\sigma(pp \to Q\bar{Q}X)}{dy_1 dy_2 d^2p_{1,t} d^2p_{2,t}} = \int \frac{d^2k_{1,t}}{\pi}\frac{d^2k_{2,t}}{\pi}\frac{1}{16\pi^2(x_1x_2s)^2}\overline{|\mathcal{M}^{\text{off-shell}}_{g^*g^*\to Q\bar{Q}}|^2} \times \delta^2(\vec{k}_{1,t}+\vec{k}_{2,t}-\vec{p}_{1,t}-\vec{p}_{2,t})\mathcal{F}_g(x_1,k_{1,t}^2,\mu_F^2) \times \mathcal{F}_g(x_2,k_{2,t}^2,\mu_F^2), \tag{2.1}$$

where $\mathcal{F}_g(x_1,k_{1,t}^2,\mu_F^2)$ and $\mathcal{F}_g(x_2,k_{2,t}^2,\mu_F^2)$ are the gluon uPDFs for both colliding hadrons and $\mathcal{M}^{\text{off-shell}}_{g^*g^*\to Q\bar{Q}}$ is the off-shell matrix element for the hard subprocess. The gluon uPDF depends on the gluon longitudinal momentum fraction x, transverse momentum squared k_t^2 of the gluons entering the hard process, and (in general) a (factorization) scale of the hard process μ_F^2. The extra integration is over the transverse momenta of the initial partons. Here, one keeps exact kinematics from the very beginning and additional hard dynamics coming from transverse momenta of incident partons. This explicit treatment of the transverse momenta makes the approach very efficient in studies of correlation observables. The two-dimensional Dirac delta function ensures momentum conservation. The gluon uPDFs must be evaluated at longitudinal momentum fractions $x_1=\frac{m_{1,t}}{\sqrt{s}}\exp(y_1)+\frac{m_{2,t}}{\sqrt{s}}\exp(y_2)$ and $x_2=\frac{m_{1,t}}{\sqrt{s}}\exp(-y_1)+\frac{m_{2,t}}{\sqrt{s}}\exp(-y_2)$, where $m_{i,t}=\sqrt{p_{i,t}^2+m_Q^2}$ are the quark/antiquark transverse masses.

The off-shell matrix elements are known explicitly only at the LO and only for limited types of $2 \to 2$ QCD processes (see, e.g., heavy quark [49], dijet [49], and Drell-Yan [50] mechanisms). Recently, higher-multiplicity processes ($2 \to 3$ and $2 \to 4$) with off-shell partons were also calculated at tree level in the context of $c\bar{c}+$ jets [22,51,52], $\gamma + c$-jet [53], $Z^0 + c/b$-jet [54], four-jet [55], and double-charm [56] production. Some first steps toward calculating NLO corrections in the k_T-factorization framework have been made for diphoton production [57,58]. There are ongoing intensive works on construction of the full NLO Monte Carlo generator for off-shell initial-state partons that are expected to be finished in the near future [59]. Another method for calculating higher-multiplicity final states is to supplement the QCD $2 \to 2$ processes with a parton shower. This was done for off-shell initial-state partons with the help of the full hadron-level Monte Carlo generator CASCADE [60]. There, dedicated transverse-momentum-dependent initial-state parton showers were introduced using backward evolution, which is not unique and needs to be matched to a given model of uPDFs.

Technically, there is a direct relation between the resummation present in uPDFs in the transverse-momentum-dependent factorization and the parton shower in the collinear framework. The popular statement is that in the k_T-factorization approach, already at leading order, some part of radiative higher-order corrections can be effectively included via uPDFs, without any additional showering procedure. However, this strictly depends on the theoretical construction of different uPDF models, in which extra emissions of soft and hard partons can be encoded. In some uPDF models the off-shell gluon can be produced from either a gluon or quark; therefore, in the k_T factorization all channels driven by $gg, q\bar{q}$, and even qg initial states are already open at leading order (in contrast to the collinear factorization). Then, when calculating the heavy-flavor production cross section via the $g^*g^* \to Q\bar{Q}$ mechanism, one could expect to effectively include contributions related to one or two (or even more) extra partonic emissions, which in some sense play the role of the initial-state parton shower.

B. Hybrid model

The LHCb measurement of $c\bar{c}$ and $b\bar{b}$ dijets is performed within the asymmetric kinematical configuration. Under the general assumption that $x_1 \gg x_2$, the cross section for the processes under consideration can also be expressed in the so-called hybrid-factorization approach, motivated by the work in Refs. [61,62]. In this framework the small-x gluon is taken to be off mass shell, the large-x gluon is treated as collinear (see the diagram in Fig. 2), and the differential cross section, e.g., for $pp \to Q\bar{Q}X$ via the $g^*g \to Q\bar{Q}$ mechanism reads

$$d\sigma_{pp\to Q\bar{Q}X} = \int d^2k_t \int \frac{dx_1}{x_1}\int dx_2 g(x_1,\mu^2) \times \mathcal{F}_{g^*}(x_2,k_t^2,\mu^2)d\hat{\sigma}_{g^*g\to Q\bar{Q}}, \tag{2.2}$$

where $g(x_1,\mu^2)$ is a collinear PDF in one proton and $\mathcal{F}_{g^*}(x_2,k_t^2,\mu^2)$ is the unintegrated gluon distribution in the

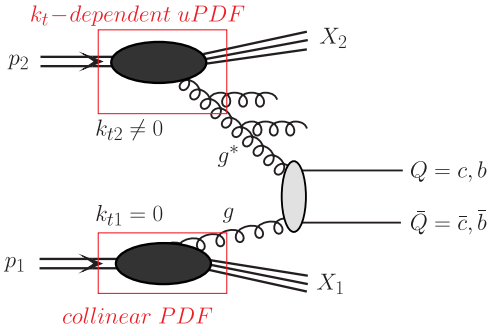

FIG. 2. Diagrammatic representation of the leading-order mechanism of heavy-flavored dijet production in the hybrid model.

second one. $d\hat{\sigma}_{g^*g\to Q\bar{Q}}$ is the hard partonic cross section obtained from the gauge-invariant tree-level off-shell amplitude. In the present paper we will not discuss the validity of the hybrid model on the theoretical level and instead concentrate only on its phenomenological application in forward production. A derivation of the hybrid factorization from the dilute limit of the color-glass condensate approach can be found in Ref. [63].

C. Unintegrated parton distribution functions

1. Ciafaloni-Catani-Fiorani-Marchesini uPDFs

The Ciafaloni-Catani-Fiorani-Marchesini (CCFM) evolution equation for the gluon, in the limits of high and low energies (small- and large-x values), is almost equivalent to the Balitsky-Fadin-Kuraev-Lipatov (BFKL) evolution equation and very similar to the Dokshitzer-Gribov-Lipatov-Altarelli-Parisi (DGLAP) evolution equation [64]. In order to correctly treat gluon coherence effects, it introduces the so-called angular ordering which is commonly considered as a great advantage of this framework.

In the leading-logarithmic approximation, the CCFM equation for the unintegrated gluon density $\mathcal{F}_g(x,k_t^2,\mu^2)$ can be written as

$$\begin{aligned}\mathcal{F}_g(x,k_t^2,\mu^2) &= \mathcal{F}_g^{(0)}(x,k_t^2,\mu_0^2)\Delta_s(\mu,\mu_0) \\ &+ \int\frac{dz}{z}\int\frac{dq^2}{q^2}\Theta(\mu-zq)\Delta_s(\mu,zq)\tilde{P}_{gg}(z,k_t^2,q^2) \\ &\times\mathcal{F}_g\left(\frac{x}{z},k_t'^2,q^2\right),\end{aligned} \tag{2.3}$$

where μ^2 is the evolution (factorization) scale which is further defined by the maximal angle allowed for gluon emission, $k_t' = q(1-z)+k_T$, and $\tilde{P}_{gg}(z,k_t^2,q^2)$ is the CCFM splitting function:

$$\begin{aligned}\tilde{P}_{gg}(z,k_t^2,q^2) &= \bar{\alpha}_s(q^2(1-z)^2)\left[\frac{1}{1-z}+\frac{z(1-z)}{2}\right] \\ &+ \bar{\alpha}_s(k_t^2)\left[\frac{1}{z}-1+\frac{z(1-z)}{2}\right]\Delta_{ns}(z,k_t^2,q^2).\end{aligned} \tag{2.4}$$

The Sudakov and non-Sudakov form factors read

$$\ln\Delta_s(\mu,\mu_0) = -\int_{\mu_0^2}^{\mu^2}\frac{d\mu'^2}{\mu'^2}\int_0^{z_M=1-\mu_0/\mu'}dz\frac{\bar{\alpha}_s(\mu'^2(1-z)^2)}{1-z}, \tag{2.5}$$

$$\begin{aligned}&\ln\Delta_{ns}(z,k_t^2,q_t^2) \\ &= -\bar{\alpha}_s(k_t^2)\int_0^1\frac{dz'}{z'}\int\frac{dq^2}{q^2}\Theta(k_t^2-q^2)\Theta(q^2-z'^2q_t^2),\end{aligned} \tag{2.6}$$

where $\bar{\alpha}_s = 3\alpha_s/\pi$.

The first term in the CCFM equation is the initial unintegrated gluon density multiplied by the Sudakov form factor. It corresponds to the contribution of nonresolvable branchings between the starting scale μ_0^2 and the current running scale μ^2. The second term describes the details of the QCD evolution expressed by the convolution of the CCFM gluon splitting function with the gluon density and the Sudakov form factor. The theta function introduces the angular-ordering condition.

The CCFM equation can be solved numerically using uPDFevolv [65], and the uPDFs for the gluon and valence quarks can be obtained for any x, k_t^2, and μ^2 values. Since only valence quarks are included in the evolution, the resulting CCFM gluon uPDF can be characterized as nearly 0-flavor scheme density. Therefore, it might be expected to be larger with respect to DGLAP-based unintegrated distributions that represent a variable-flavor-number-scheme framework.

Within the CCFM approach the parton transverse momentum is allowed to be larger than the scale μ^2. This useful feature allows to effectively take into account higher-order radiative corrections, which correspond to the initial-state real gluon emissions that are resummed into the uPDFs.

The CCFM approach for the gluon uPDF was successfully used in the past to describe B-meson and $b\bar{b}$-dijet production data taken by the D0 and CDF collaborations at Tevatron [66] as well as by the CMS Collaboration at the LHC [25].

2. Parton branching uPDFs

The parton-branching (PB) method, introduced in Refs. [67,68], provides an iterative solution for the evolution of both collinear and transverse-momentum-dependent parton distributions. Within this novel method the splitting kinematics at each branching vertex stays under full control during the QCD evolution. Here, soft-gluon emission in the region $z\to 1$ and transverse momentum recoils in the parton branchings along the QCD cascade are taken into account simultaneously. Therefore, the PB approach allows for a natural determination of the uPDFs, as the transverse momentum at every branching vertex is known. It agrees with the usual methods to solve the DGLAP equations, but also provides the possibility to apply angular ordering instead of the standard ordering in virtuality.

Within the PB method, a soft-gluon resolution scale parameter z_M is introduced into the QCD evolution equations that distinguishes between nonresolvable and resolvable emissions. These two types of emissions are further treated with the help of the Sudakov form factors

$$\Delta_a(z_M,\mu^2,\mu_0^2) = \exp\left(-\sum_b\int_{\mu_0^2}^{\mu^2}\frac{d\mu'^2}{\mu'^2}\int_0^{z_M}dzzP_{ba}^{(R)}(\alpha_s,z)\right) \tag{2.7}$$

and resolvable splitting probabilities $P_{ba}^{(R)}(\alpha_s, z)$, respectively. Here a and b are flavor indices, α_s is the strong coupling, z is the longitudinal at a scale being a function of μ'^2, z is the longitudinal momentum splitting variable, and $z_M < 1$ is the soft-gluon resolution parameter. Then, by connecting the evolution variable μ in the splitting process $b \to ac$ with the angle Θ of the momentum of particle c with respect to the beam direction, the known angular-ordering relation $\mu = |q_{t,c}|/(1-z)$ is obtained, which ensures the quantum coherence of softly radiated partons.

The PB evolution equations with the angular-ordering condition for unintegrated parton densities $\mathcal{F}_a(x, k_t, \mu^2)$ are given by [67]

$$\mathcal{F}_a(x, k_t, \mu^2) = \Delta_a(\mu^2)\mathcal{F}_a(x, k_t, \mu_0^2) + \sum_b \int \frac{d^2q_t'}{\pi q_t'^2}\frac{\Delta_a(\mu^2)}{\Delta_a(q_t'^2)}\Theta(\mu^2 - q_t'^2)\Theta(q_t'^2 - \mu_0^2) \times \int_x^{z_M}\frac{dz}{z}P_{ab}^{(R)}(\alpha_s, z)\mathcal{F}_b\left(\frac{x}{z}, k_t + (1-z)q_t', q_t'^2\right). \tag{2.8}$$

Here, the starting distribution for the uPDF evolution is taken in the factorized form as a product of a collinear PDF fitted to the precise deep inelastic scattering data and an intrinsic transverse momentum distribution in a simple Gaussian form. Unlike the CCFM parton distributions, the PB densities have the strong normalization property

$$\int \mathcal{F}_a(x, k_t, \mu^2)dk_t = f_a(x, \mu^2), \tag{2.9}$$

and therefore well reproduce modern collinear PDFs after integrating out their k_t dependence. The PB uPDFs, including those for gluons and quarks, can be calculated by an iterative Monte Carlo method and are characterized by a steep drop of the parton densities at $k_t^2 > \mu^2$, again in contrast to the CCFM unintegrated distributions.[1]

There are two basic sets of parton-branching uPDFs, PB-NLO-2018-set1 and PB-NLO-2018-set2, which correspond to different choices of the parameters of the initial distributions [68]. Both, including uncertainties, are available in TMDlib [70] and were previously used to describe the LHCb data on forward production of open-charm mesons [22,23].

3. Kimber-Martin-Ryskin/Martin-Ryskin-Watt uPDFs

Another DGLAP-based prescription frequently used in phenomenological studies for unintegrated parton densities is the Kimber-Martin-Ryskin (KMR) approach [71–73]. In particular, it has been successfully used for heavy-flavor production at the LHC, including inclusive charm mesons and baryons [21,74], charm-anticharm meson pairs [21,26], double- and triple-charm mesons [31,75–77], charm mesons associated with jets [51,52], and B mesons and $b\bar{b}$ dijets [25].

[1]Incorporating CCFM effects into the PB method was only recently attempted for the first time [69].

According to this approach, the unintegrated gluon distribution is given by the following formula:

$$f_g(x, k_t^2, \mu^2) \equiv \frac{\partial}{\partial \log k_t^2}[g(x, k_t^2)T_g(k_t^2, \mu^2)] = T_g(k_t^2, \mu^2)\frac{\alpha_S(k_t^2)}{2\pi}\sum_b \int_x^1 dz P_{gb}(z) b\left(\frac{x}{z}, k_t^2\right). \tag{2.10}$$

This formula makes sense for $k_t > \mu_0$, where $\mu_0 \sim 1$ GeV is the minimum scale for which DGLAP evolution of the conventional collinear gluon PDF, $g(x, \mu^2)$, is valid. A similar expression can also be written for quarks.

The virtual (loop) contributions may be resummed to all orders by the Sudakov form factor

$$T_g(k_t^2, \mu^2) \equiv \exp\left(-\int_{k_t^2}^{\mu^2}\frac{\mathrm{d}\kappa_t^2}{k_t^2}\frac{\alpha_S(\kappa_t^2)}{2\pi}\sum_b \int_0^1 \mathrm{d}z z P_{bg}(z)\right), \tag{2.11}$$

which gives the probability of evolving from a scale k_t to a scale μ without parton emission. The exponent of the gluon Sudakov form factor can be simplified using the identity $P_{qg}(1-z) = P_{qg}(z)$. Then, the gluon Sudakov form factor reads

$$T_g(k_t^2, \mu^2) = \exp\left(-\int_{k_t^2}^{\mu^2}\frac{\mathrm{d}\kappa_t^2}{k_t^2}\frac{\alpha_S(\kappa_t^2)}{2\pi}\left(\int_0^{1-\Delta}\mathrm{d}z z P_{gg}(z) + n_F\int_0^1 \mathrm{d}z P_{qg}(z)\right)\right), \tag{2.12}$$

where n_F is the active number of flavors of the quark-antiquark pairs into which the gluon may split. Due to the presence of the Sudakov form factor in the KMR prescription, only the last emission generates transverse momentum of the gluons initiating hard scattering.

In the above equation the variable Δ introduces a restriction of the phase space for gluon emission and is crucial for the final shape and characteristics of the unintegrated density. In Ref. [71] the cutoff Δ was set in accordance with the strong ordering in transverse momenta of the real parton emission in the DGLAP evolution,

$$\Delta = \frac{k_t}{\mu}. \tag{2.13}$$

This corresponds to the original KMR prescription where one always has the restriction $k_t^2 < \mu_F^2$ and the Sudakov form factor always satisfies the $T_g(k_t^2, \mu^2) < 1$ condition.

The prescription for the cutoff Δ was further modified in Refs. [72,73] to account for the angular ordering in parton emissions in the spirit of the CCFM evolution,

$$\Delta = \frac{k_t}{k_t + \mu}. \tag{2.14}$$

This modification leads to a bigger upper limit for k_t than in the DGLAP scheme and opens the $k_t^2 > \mu_F^2$ region. In this extra kinematical regime one gets $T_g(k_t^2, \mu^2) > 1$, which contradicts its interpretation as the probability of no real emission. Thus, the Sudakov form factor is usually set equal to 1 in that domain. For transparency, here the modified KMR model will be referred to as the Martin-Ryskin-Watt (MRW) model [73].

Different definitions of the ordering cutoff lead to significant differences between the two models. In the KMR model the $k_t^2 > \mu_F^2$ region is forbidden, while in the MRW case the $k_t^2 > \mu_F^2$ contributions are directly allowed (see, e.g., the detailed discussion in Ref. [78]). In the MRW model large k_t tails appear in both quark and gluon densities, in contrast to the KMR case. In the numerical calculations below we use the MMHT2014 [79] collinear PDFs to calculate both the KMR and MRW unintegrated densities.

4. Kutak-Sapeta uPDFs

An alternative approach to those presented above has been applied in the Kutak-Sapeta (KS) model [62,80] for the gluon uPDF. There the unintegrated gluon density is obtained from the unified framework of the Balitsky-Kovchegov (BK) [81–83] and DGLAP evolution equations and then fitted to combined HERA data. This framework is a continuation of the model presented some time ago in Ref. [84] for unified BFKL-DGLAP evolution. It extends the ideas presented there by taking into account the nonlinear (or gluon saturation) effects in the QCD evolution. In order to account for some effects related to the saturation of gluons, the unified BFKL-DGLAP evolution equation is supplemented with the nonlinear term in the BK form. Thus, the authors obtained the so-called modified BK equation in which the unified linear part deals with partial resummation of the next-to-leading-logarithmic approximation corrections and the nonlinear term is taken in the basic leading-logarithmic approximation approach.

According to this approach the improved nonlinear equation for the unintegrated gluon density, written in momentum space, reads as follows:

$$\mathcal{F}_g(x,k^2) = \mathcal{F}_g^{(0)}(x,k^2) + \frac{\alpha_s(k^2)N_c}{\pi}\int_x^1 \frac{dz}{z}\int_{k_0^2}^{\infty}\frac{dl^2}{l^2}\left\{\frac{l^2\mathcal{F}(\frac{x}{z},l^2) - k^2\mathcal{F}(\frac{x}{z},k^2)}{|l^2-k^2|} + \frac{k^2\mathcal{F}(\frac{x}{z},k^2)}{|4l^4+k^4|^{\frac{1}{2}}}\right\}$$
$$- \frac{2\alpha_s^2(k^2)}{\rho^2}\left[\left(\int_{k^2}^{\infty}\frac{dl^2}{l^2}\mathcal{F}(x,l^2)\right)^2 + \mathcal{F}(x,k^2)\int_{k^2}^{\infty}\frac{dl^2}{l^2}\ln\left(\frac{l^2}{k^2}\right)\mathcal{F}(x,l^2)\right], \tag{2.15}$$

where ρ is the radius of the hadronic target and $\mathcal{F}_g^{(0)}(x,k^2)$ is the starting distribution. The linear part of the equation is given by the BFKL kernel, while the nonlinear part is proportional to the triple Pomeron vertex which allows for the recombination of gluons.

The basic model of the KS gluon uPDF [62] was further extended by introducing a factorization scale dependence [80] of the originally scale-independent density $\mathcal{F}_g(x,k^2)$. The scale dependence is obtained as follows:

$$\mathcal{F}_g(x,k^2,\mu^2) := \theta(\mu^2-k^2)T_s(\mu^2,k^2)\frac{xg(x,\mu^2)}{xg_{hs}(x,\mu^2)} \times \mathcal{F}_g(x,k^2) + \theta(k^2-\mu^2)\mathcal{F}_g(x,k^2), \tag{2.16}$$

where

$$xg_{hs}(x,\mu^2) = \int^{\mu^2} dk^2 T_s(\mu^2,k^2)\mathcal{F}_g(x,k^2), xg(x,\mu^2) = \int^{\mu^2} dk^2 \mathcal{F}_g(x,k^2) \tag{2.17}$$

and the Sudakov form factor assumes the form

$$T_s(\mu^2,k^2) = \exp\left(-\int_{k^2}^{\mu^2}\frac{dk'^2}{k'^2}\frac{\alpha_s(k'^2)}{2\pi}\sum_{a'}\int_0^{1-\Delta}dz' P_{a'a}(z')\right), \tag{2.18}$$

where $\Delta = \frac{\mu}{\mu+k}$ and $P_{a'a}$ is a splitting function with subscripts $a'a$ specifying the type of transition.

In the numerical calculations below we apply both the KS-linear and KS-nonlinear gluon uPDF sets as implemented in TMDlib. Phenomenological applications of these densities are limited to the $x < 10^{-2}$ kinematic domain and therefore they can be applied only when considering small-x effects. The KS gluon uPDFs are frequently used within the hybrid approach and are found to be very useful, especially in phenomenological studies of forward particle production that are taking place in highly asymmetric kinematical configurations. Recently, the densities have been examined in the context of forward jet, forward-forward dijet, and central-forward dijet production at the LHC (see, e.g., Refs. [85–88]).

III. NUMERICAL RESULTS

In this section we present a variety of numerical results of the theoretical models described above for inclusive production of the $c\bar{c}$-dijets at the LHC. The theoretical predictions are confronted with corresponding experimental data from the LHCb experiment [46] collected recently at $\sqrt{s} = 13$ TeV. In the first step we show results obtained within the exact k_T-factorization framework, and then we carefully discuss the kinematics behind the processes under consideration. Next, we focus on the predictions based on the hybrid model. We show explicitly the role of the large-x behavior of gluon densities for a satisfactory description of the LHCb data. The large-x part of the gluon distributions is crucial for better understanding the QCD dynamics behind the considered reaction. Finally, we discuss the scale uncertainty of our predictions and

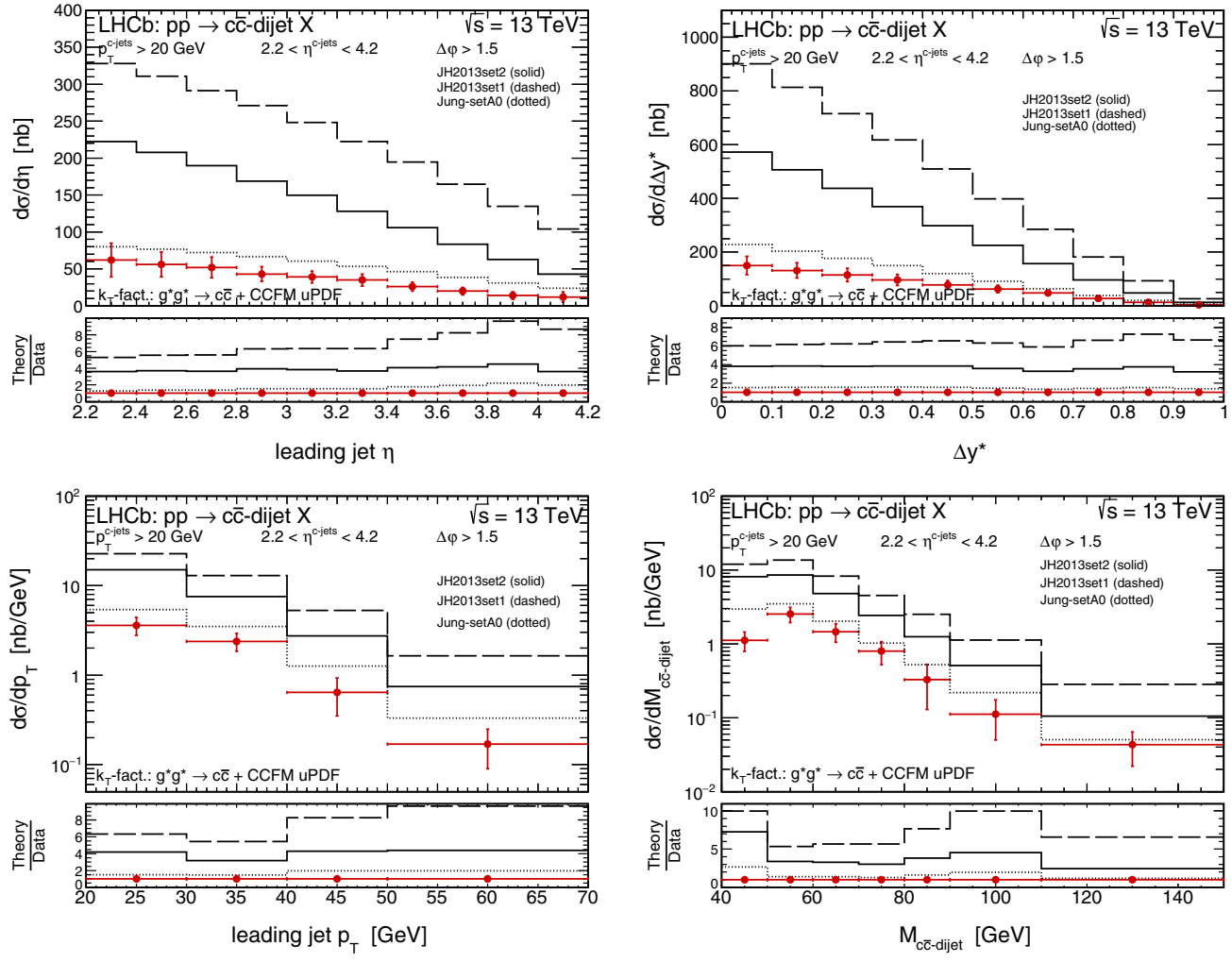

FIG. 3. Differential cross sections for forward production of $c\bar{c}$ dijets in pp scattering at $\sqrt{s} = 13$ TeV as functions of the leading jet η (top left), rapidity difference Δy^* (top right), leading jet p_T (bottom left), and dijet invariant mass $M_{c\bar{c}-\mathrm{dijet}}$ (bottom right). Here the dominant pQCD $g^*g^* \to c\bar{c}$ mechanism is taken into account. The theoretical histograms correspond to the k_T-factorization calculations obtained with the CCFM uPDFs.

$R = \frac{c\bar{c}}{b\bar{b}}$ dijet cross-section ratio as a function of a few kinematical variables. For completeness, we also present a direct comparison to the corresponding results of calculations based on the collinear framework.

For the sake of clarity, in this section we skip the presentation of our numerical results for $b\bar{b}$ dijets and move it to Appendices A and B. We wish to reduce here a number of figures with numerical predictions in order to ensure that the message of the paper is clear and not diluted by the numerous repeated results. Considering the acceptance of the LHCb detector, one should not expect large effects related to the heavy-quark mass. Although the experimental data show some small but visible difference between the cross sections for charm and bottom flavors, our theoretical predictions are almost insensitive to the heavy-quark mass. The difference between our theoretical histograms for charm and bottom dijets is extremely small. We will discuss this issue in more detail in the following when presenting results for the charm-to-bottom dijet ratio data ($R = \frac{c\bar{c}}{b\bar{b}}$).

For the same reason, we provide a dedicated discussion of the scale uncertainties of our predictions in Appendix C, as well as a supplementary discussion on finite jet size effects in Appendix D.

A. Predictions of the standard k_T-factorization framework

As a default set in the numerical calculations below, we take the renormalization/factorization scales $\mu^2 = \mu_R^2 = \mu_F^2 = \sum_{i=1}^{n} \frac{m_{ti}^2}{n}$ (averaged transverse mass of the given final state) and the charm- and bottom-quark masses $m_c = 1.5$ GeV and $m_b = 4.75$ GeV, respectively. The strong-coupling constant $\alpha_s(\mu_R^2)$ at NLO is taken from the MMHT2014 PDF routines.

For the CCFM uPDFs we always set the factorization scale to $\mu^2 = M_{Q\bar{Q}}^2 + p_T^{Q\bar{Q}}$, where $M_{Q\bar{Q}}$ is the invariant mass of the $Q\bar{Q}$ system (or energy of the scattering

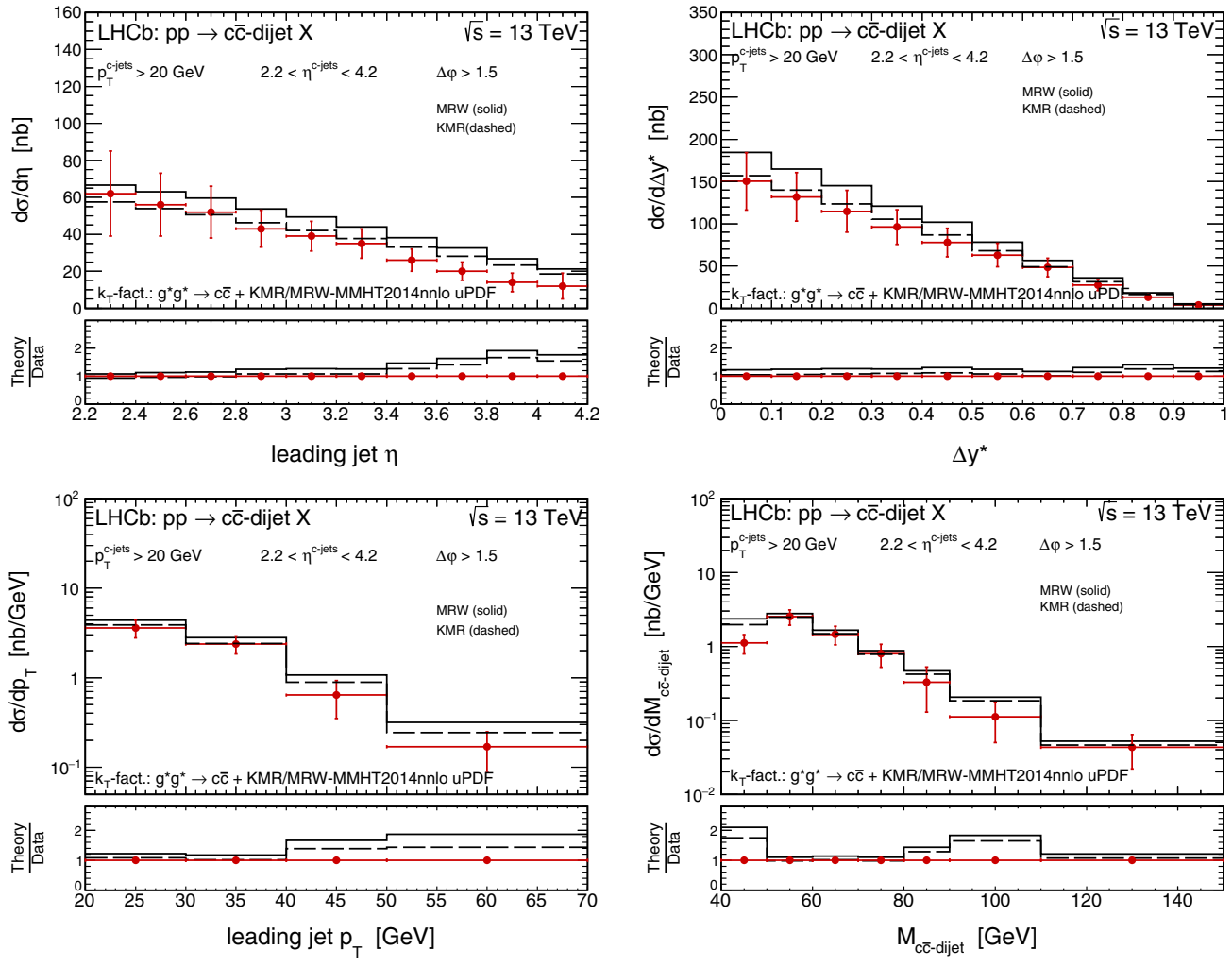

FIG. 4. Same as in Fig. 3 but here the KMR and the MRW uPDFs are used.

subprocess) and $p_T^{Q\bar{Q}}$ is the transverse momentum of the $Q\bar{Q}$ pair (or of the incoming off-shell gluon pair). This has to be applied as a consequence of the CCFM evolution algorithm.

Here and in the following only the pQCD gluon-gluon fusion $g^*g^* \to Q\bar{Q}$ mechanism that is dominant at high energies is taken into account. We have numerically checked that the annihilation $q^*\bar{q}^* \to Q\bar{Q}$ mechanism is negligible here and can be safely neglected.

We start by presenting the numerical results for forward production of $c\bar{c}$ dijets in pp scattering at $\sqrt{s} = 13$ TeV. In Fig. 3 we show the corresponding differential cross sections as functions of the leading jet η (top left panels), rapidity difference Δy^* (top right panels), leading jet p_T (bottom left panels), and dijet invariant mass $M_{c\bar{c}-\text{dijet}}$ (bottom right panels). The theoretical histograms are obtained with the k_T-factorization approach using three different sets of the CCFM uPDFs: JH2013set1 (dashed), JH2013set2 (solid), and Jung-setA0 (dotted). We observe that both of the most recent CCFM uPDF sets, i.e., JH2013set1 and set2 significantly overshoot the experimental data in the whole kinematic range probed by the LHCb experiment. The results of the k_T factorization with the JH2013set2 uPDF are slightly closer to the data points than those obtained with the JH2013set1 uPDF set. The JH-2013-set1 gluon density is determined from the fit to inclusive F_2 HERA data only when the JH-2013-set2 set is determined from the fit to both $F_2^{(\text{charm})}$ and F_2 data; however, even for the latter case, here the discrepancy between the predictions and the LHCb measurement is huge. Surprisingly, the Jung setA0 gluon density (that is a bit older set of the CCFM gluon uPDF than the JH-2013 sets) leads to a much better description of the experimental data and seems to only slightly overestimates the distributions measured by the LHCb.

In Fig. 4 we show similar k_T-factorization results, but here we use the KMR (dashed histograms) and MRW (solid

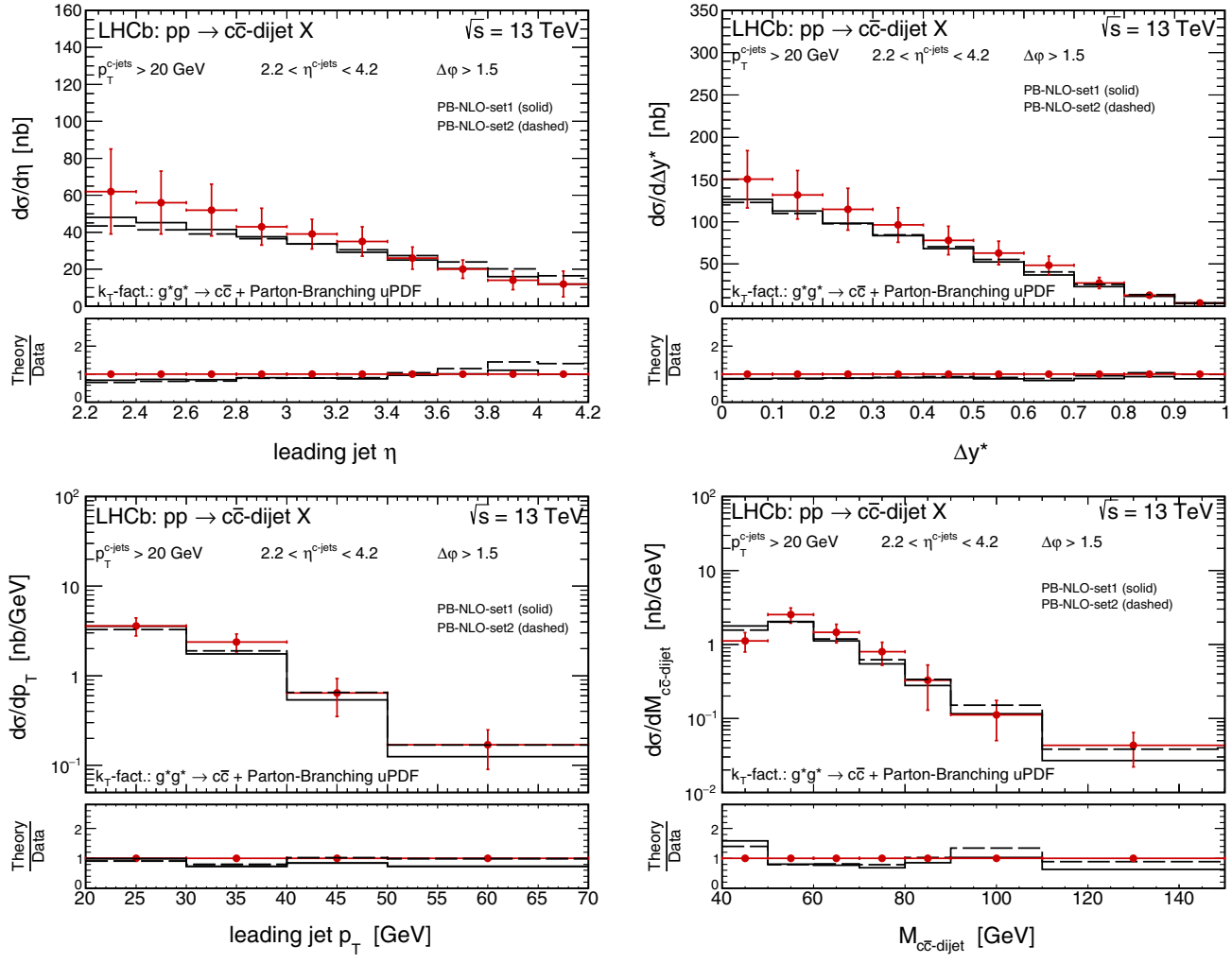

FIG. 5. Same as in Fig. 3 but here the parton-branching uPDFs are used.

histograms) gluon uPDFs. Both models seem to reasonably well describe the LHCb data. The histograms that represent the KMR predictions show a slightly better agreement with the data. This is especially visible for the leading jet η and Δy^* distributions which are displayed on a linear scale. However, the effect is not significant for the overall picture and does not strongly disfavor the MRW gluon density here.

Next we examine the parton-branching gluon uPDFs against the LHCb data. In Fig. 5 we present our predictions for the PB-NLO-set1 (solid) and PB-NLO-set2 (dashed) gluon densities. As opposed to the CCFM and KMR/MRW

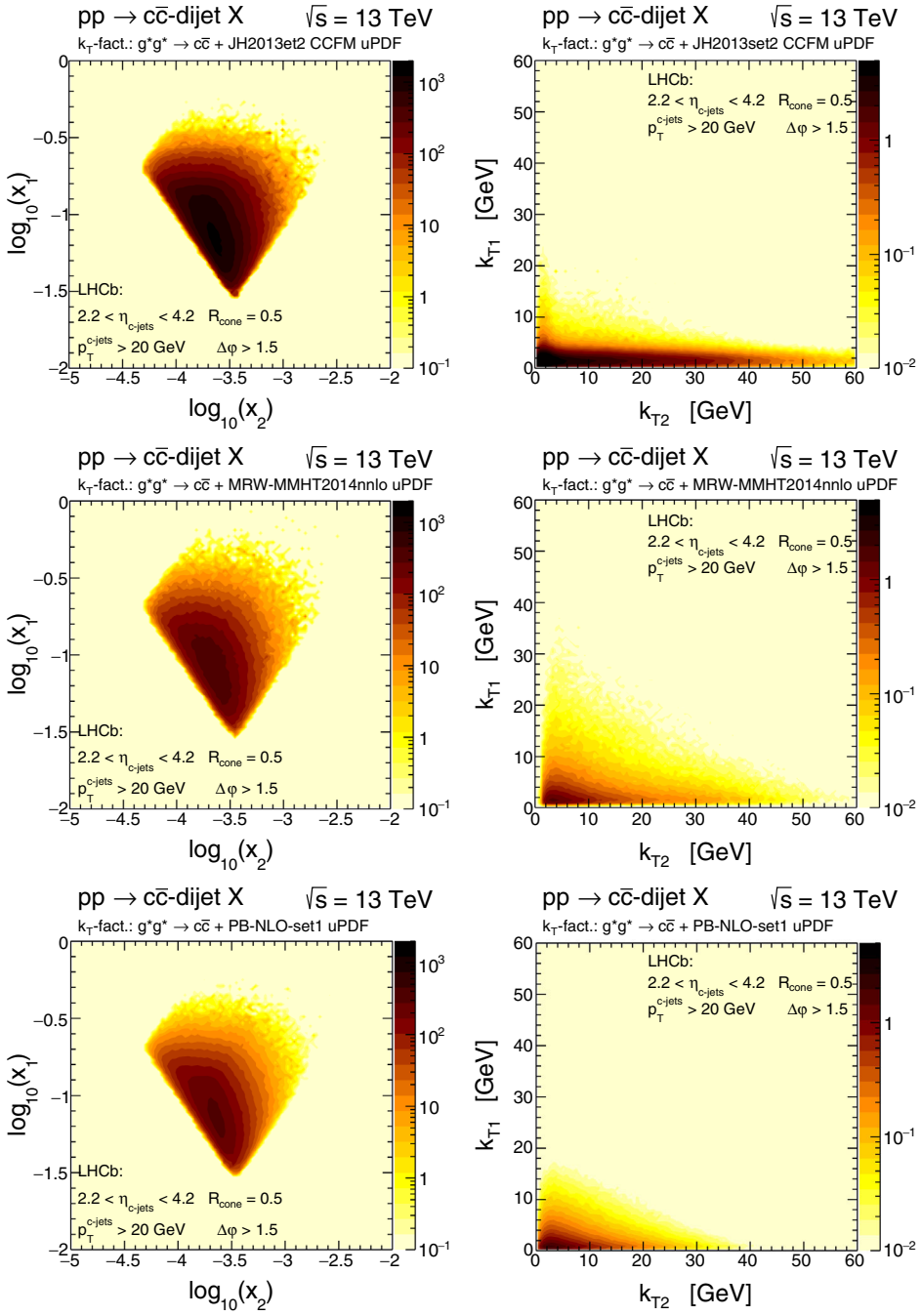

FIG. 6. Double differential cross sections for forward production of $c\bar{c}$ dijets in pp scattering at $\sqrt{s} = 13$ TeV probed in the LHCb experiment [46] as functions of the longitudinal momentum fractions $\log_{10}(x_1) \times \log_{10}(x_2)$ (left panels) and initial gluon transverse momenta $k_{t1} \times k_{t2}$ (right panels). The top, middle, and bottom panels correspond to the JH2013set2 CCFM, MRW-MMHT2014nnlo, and PB-NLO-set1 gluon uPDFs, respectively.

cases, here a slight tendency to underestimate the data points appears. However, both of the gluon densities provide a very good description of the measured distributions and lead to very similar results. A small missing strength is observed only at smaller values of the leading jet η and some differences between the two predictions are found only at large leading jet p_T's and large dijet invariant masses $M_{c\bar{c}-\mathrm{dijet}}$. The PB-NLO-set2 density seems to reproduce slopes of the distributions a bit better than the PB-NLO-set1 one. The two gluon uPDF models differ in the value of the starting evolution scale as well as in the argument of α_S. In the set1 case, the integrated parton density and the initial parameters are the same as those obtained using the HERAPDF2.0 PDF. In the set2 case, the

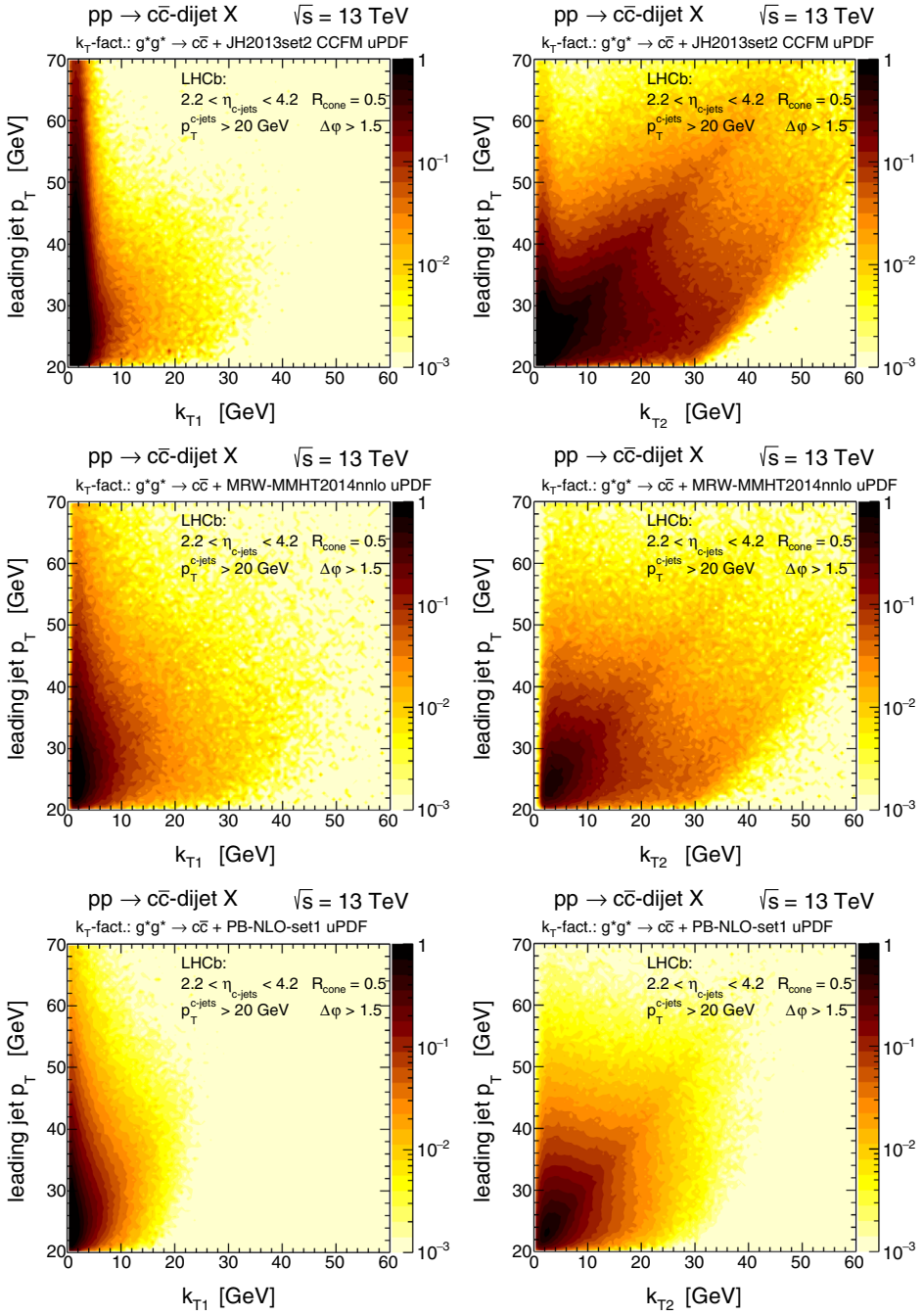

FIG. 7. Same as in Fig. 6 but here as functions of the leading c-jet transverse momentum and the initial gluon transverse momenta: $p_T \times k_{t1}$ (left panels) and $p_T \times k_{t2}$ (right panels).

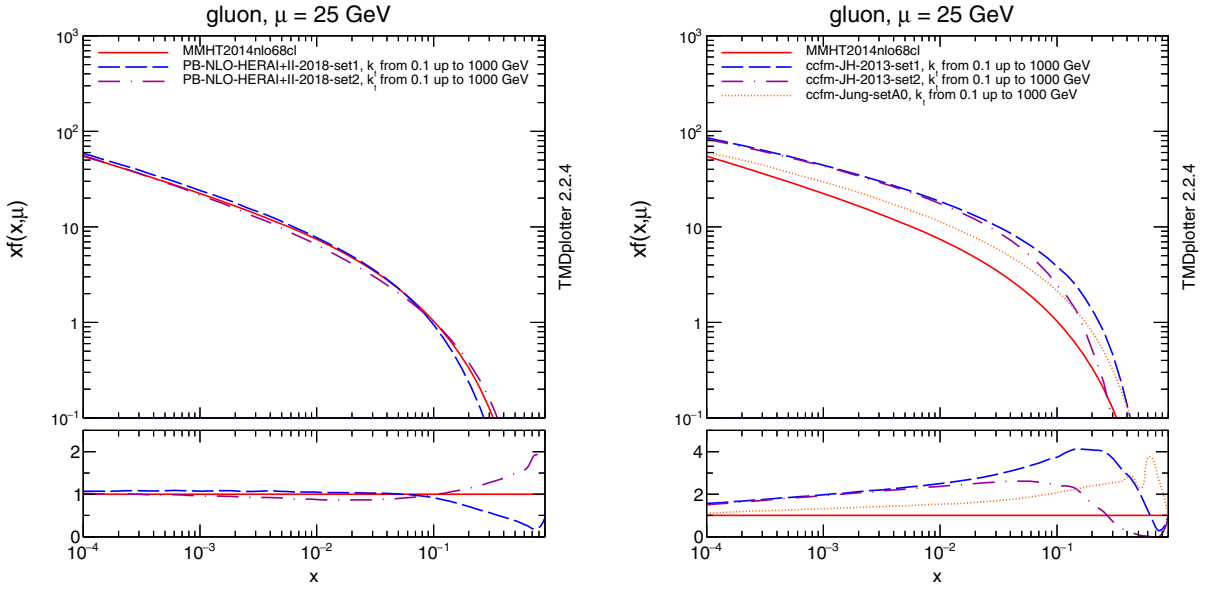

FIG. 8. Gluon uPDFs integrated over the transverse momentum k_t as functions of the longitudinal momentum fraction x at a given scale $\mu = 25$ GeV, relevant for the process under consideration. The left and right panels correspond to the parton-branching and CCFM gluon uPDFs, respectively. As a reference the collinear MMHT2014nlo68cl gluon PDF is also shown.

parameters are slightly modified and thus the integrated parton distributions do not fully reproduce the collinear ones. However, in both cases a reasonably good fit to HERA data is obtained.

B. Kinematics of the process probed by the LHCb experiment

In the previous section we have shown that within the k_T-factorization approach some of the popular gluon uPDF models have difficulties with a reasonable description of the LHCb data on the forward production of heavy-flavored dijets. In order to identify the possible reasons for this failure we wish to carefully illustrate the kinematics behind the considered process as probed by the LHCb experiment.

In Fig. 6 we present the double differential cross sections for forward production of $c\bar{c}$ dijets in pp scattering at $\sqrt{s} = 13$ TeV probed in the LHCb experiment as functions of the longitudinal momentum fractions $\log_{10}(x_1) \times \log_{10}(x_2)$ (left panels) and initial gluon transverse momenta $k_{t1} \times k_{t2}$ (right panels). The top, middle, and bottom panels correspond to the JH2013set2 CCFM, MRW-MMHT2014nnlo, and PB-NLO-set1 gluon uPDFs, respectively. It is clear now that we deal here with asymmetric configuration and probe the longitudinal momentum fractions in two different regions. On the one side x_1 is large with the maximum of the cross section around 10^{-1} and on the other side x_2 is much smaller with the maximum in the $10^{-4} < x_2 < 10^{-3}$ range. At the same time, the large-x gluon has rather small transverse momenta $k_{t1} \lesssim 5$ GeV, while the small-x gluon takes much larger k_{t2} values with the maximal range depending on the gluon uPDF model. The largest tail in k_{t2} is observed for the case of the CCFM density, while the parton-branching model leads to the smallest one.

It is also interesting to see how the initial transverse momenta of incoming gluons k_t contribute to the leading jet p_T. The mutual relation between the two variables is presented in Fig. 7. The leading jet p_T distribution in the range $20 < p_T < 50$ GeV is driven by both gluons' incident transverse momenta. On the other hand, the hardest part of the leading jet spectrum, i.e., $p_T > 50$ GeV, is dominated by the contribution from the large-x gluon.

C. Large-x behavior of the gluon uPDFs

As we have shown in the previous section, within the present study one has to deal with gluon distributions for large- and small-x simultaneously. The unintegrated densities are usually devoted to the small-x region where they can be safely used; however, the large-x behavior is challenging and might not be under full theoretical control. At large x one might expect that a given uPDF model should closely reproduce well-known collinear PDFs when integrating out the k_t dependence. Here we wish to take a closer look at this issue.

In Fig. 8 we present the gluon uPDFs integrated over the transverse momentum k_t as functions of the longitudinal momentum fraction x at a given scale $\mu = 25$ GeV, relevant for the process under consideration. The left and right panels correspond to the parton-branching and CCFM gluon uPDFs, respectively. As a reference the collinear MMHT2014nlo68cl gluon PDF is also shown. We find that the parton-branching uPDF reproduces the

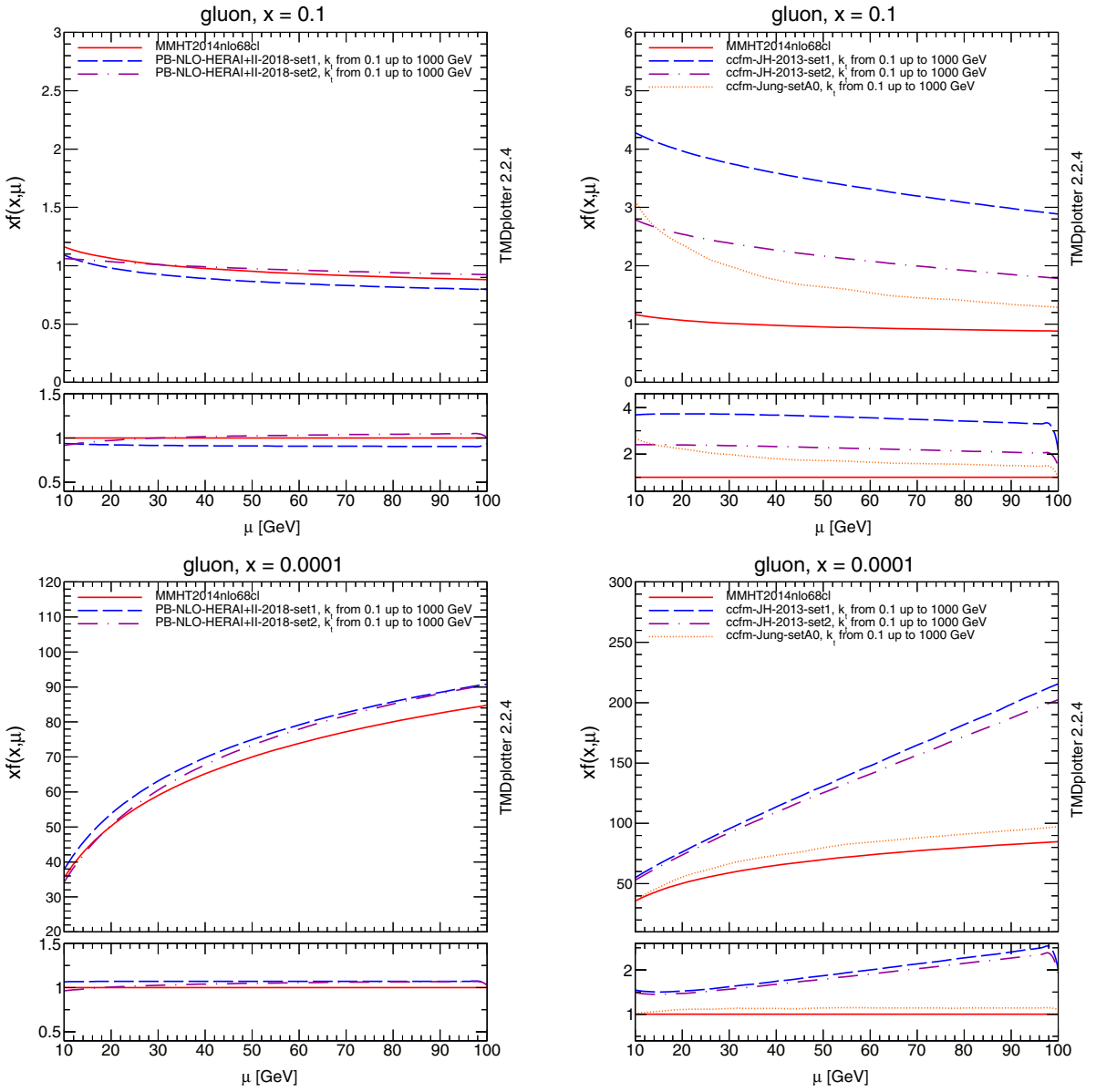

FIG. 9. Gluon uPDFs integrated over the transverse momentum k_t as functions of the factorization scale μ for a given longitudinal momentum fraction x. The left and right panels correspond to the parton-branching and CCFM gluon uPDFs, respectively. The top panels are obtained for $x = 10^{-1}$ and the bottom ones for $x = 10^{-4}$. As a reference the collinear MMHT2014nlo68cl gluon PDF is also shown.

collinear PDF very well, while for the CCFM uPDFs this is not the case.

In Fig. 9 we show the gluon uPDFs integrated over the transverse momentum k_t as functions of the factorization scale μ for a given longitudinal momentum fraction x. The left and right panels correspond to the parton-branching and CCFM gluon uPDFs, respectively. The top panels are obtained for $x = 10^{-1}$ and the bottom ones for $x = 10^{-4}$. As a reference the collinear MMHT2014nlo68cl gluon PDF is also shown. Here we see that at large x the relation between the integrated gluon uPDFs and the collinear gluon PDF does not change with the scale μ. On the other hand, the integrated gluon uPDFs grow faster with the scale than their collinear counterparts. This effect is especially visible in the case of the JH2013 CCFM uPDF sets.

Having shown rather technical issues within the full k_T-factorization approach in the following we shall consider also the hybrid-factorization approach.

D. Predictions of the hybrid-factorization framework

All off the calculations below, preformed within the hybrid model, are done using the collinear MMHT2014nlo68cl

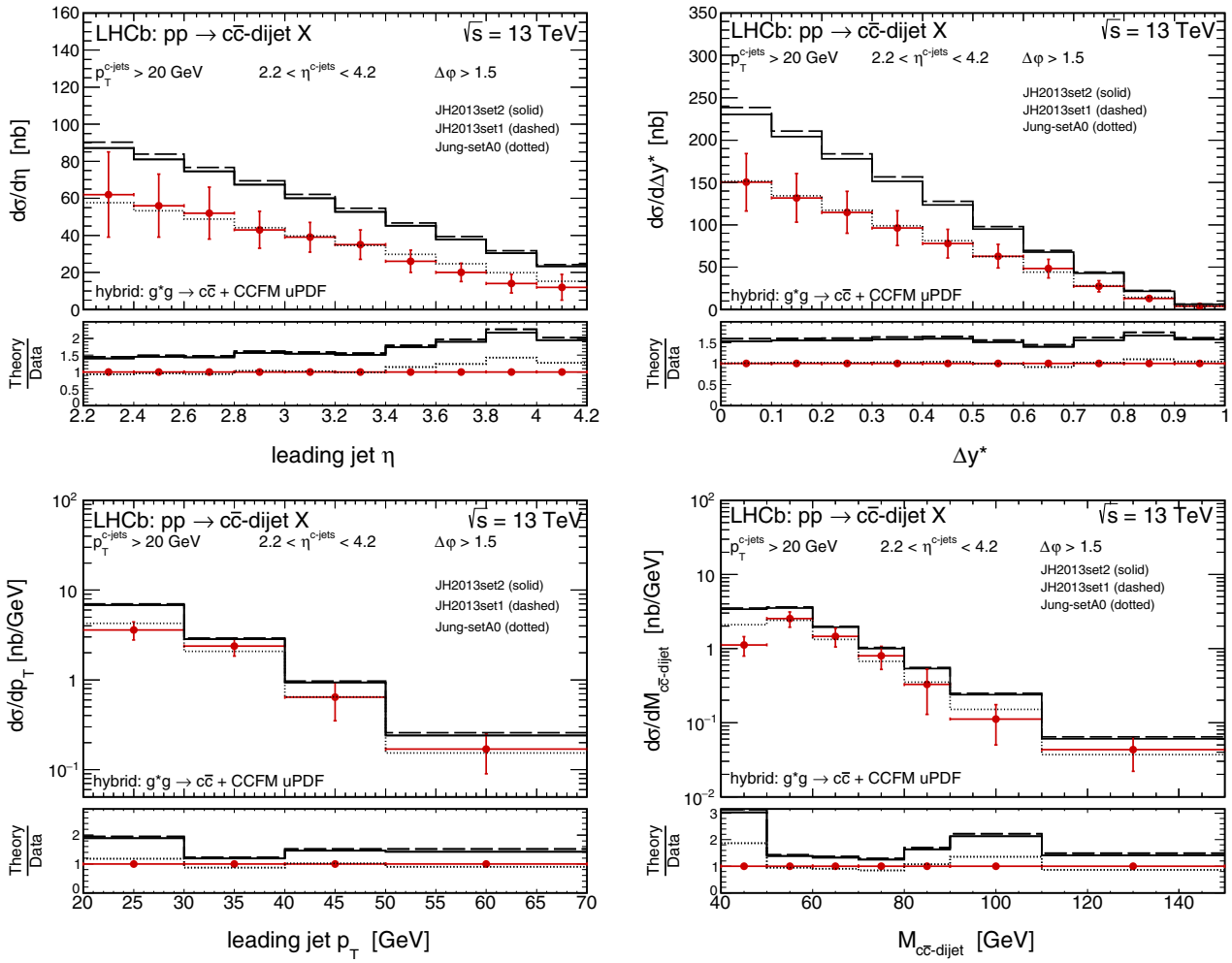

FIG. 10. Differential cross sections for the forward production of $c\bar{c}$ dijets in pp scattering at $\sqrt{s} = 13$ TeV as functions of the leading jet η (top left), rapidity difference Δy^* (top right), leading jet p_T (bottom left), and dijet invariant mass $M_{c\bar{c}-\mathrm{dijet}}$ (bottom right). Here the dominant pQCD $g^*g \to c\bar{c}$ mechanism is taken into account. The theoretical histograms correspond to the hybrid model calculations obtained with the CCFM uPDFs.

gluon PDF on the large-x side. We have numerically checked that at large x there is no significant difference between different gluon PDF sets at NLO, given in the literature by different PDF groups.

The results of the hybrid model are shown in an analogous manner as for the full k_T factorization. We start with the forward production of $c\bar{c}$ dijets in pp scattering at $\sqrt{s} = 13$ TeV. In Fig. 10 we show the corresponding differential cross sections as functions of the leading jet η (top left panels), rapidity difference Δy^* (top right panels), leading jet p_T (bottom left panels), and dijet invariant mass $M_{c\bar{c}-\mathrm{dijet}}$ (bottom right panels). The theoretical histograms are obtained for the interaction of off-shell small-x and on-shell large-x gluon distributions using three different sets of CCFM uPDFs: JH2013set1 (dashed), JH2013set2 (solid), and Jung-setA0 (dotted). We observe that within the hybrid approach the discrepancies between predictions and experimental data decrease with respect to the case of the full k_T-factorization calculations. Within the hybrid factorization and the Jung setA0 gluon uPDF we get an excellent description of the experimental distributions. In turn, here the JH2013 sets of the CCFM gluon uPDFs overestimate the data points by less than a factor of 2 only, which is also a significant improvement.

A similar effect is also observed in the case of the KMR/MRW uPDF. As can be seen in Fig. 11, using the hybrid approach leads to better agreement with the data and removes a slight tendency to overshoot the data, reported previously in the full k_T-factorization case.

On the other hand, the hybrid model results obtained with the parton-branching uPDFs show an opposite effect (see Fig. 12). Here we observe a small enhancement of the

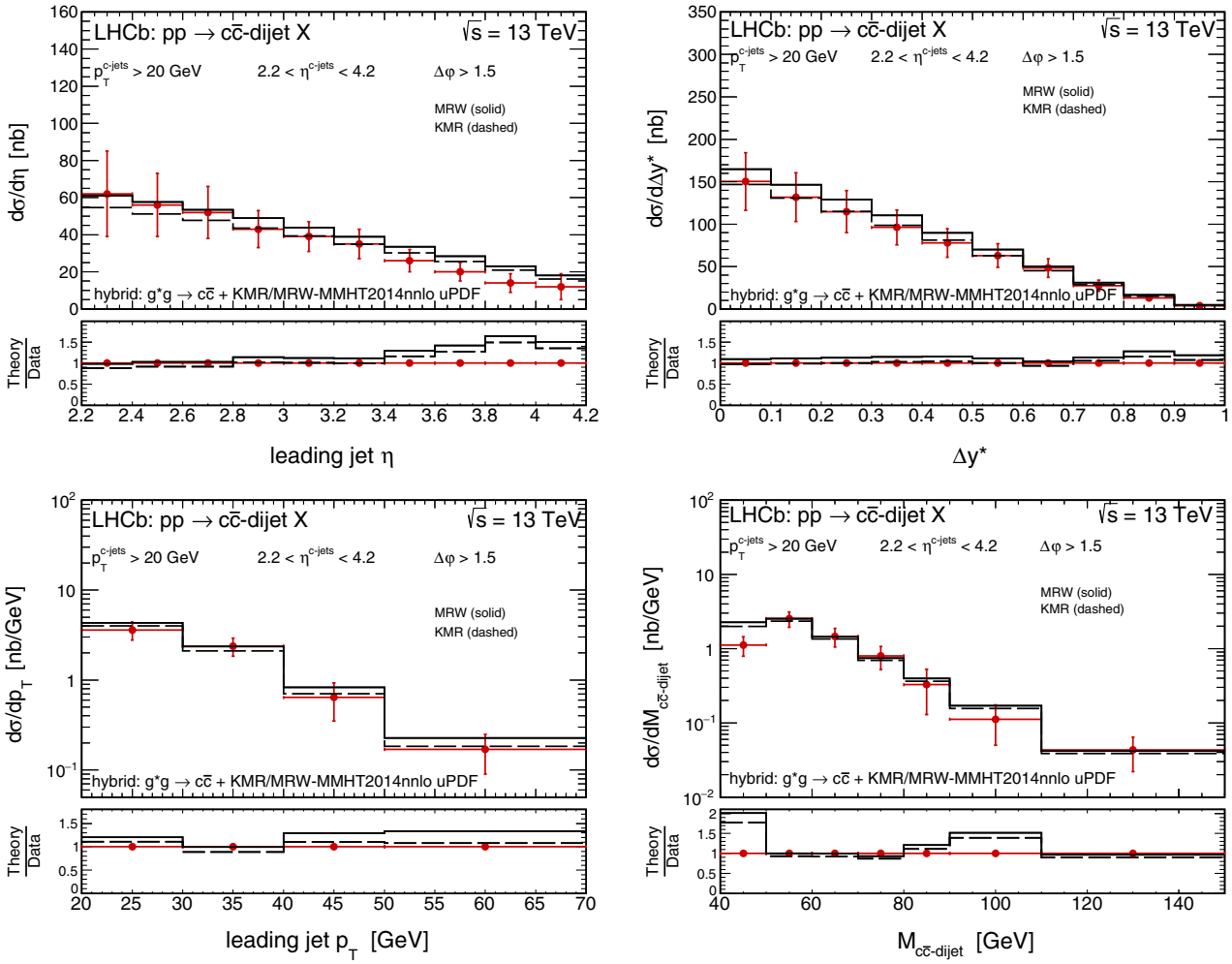

FIG. 11. Same as in Fig. 10 but here the KMR and MRW uPDFs are used.

cross section but it is heading in a good direction and improves the agreement with the experimental data, resulting in an excellent description of all four measured differential distributions.

A very good agreement between the theoretical results and the experimental data sets is also obtained for the KS-linear and KS-nonlinear gluon uPDFs (see Fig. 13). We observe that within the probed region of the phase space both parametrizations of the KS gluon densities lead to a similar cross sections. Within the present precision the LHCb $c\bar{c}$ dijet data seems to be not sensitive to the saturation effects. Here the size of the effects related to nonlinear evolution is quite small-in principle visibly smaller than the experimental uncertainties.

E. Charm/bottom dijet ratio

To summarize the previous subsection, we conclude that the best agreement between the LHCb heavy-flavored dijet data and the predictions of the hybrid model can be obtained for the PB-NLO-set1 uPDF. However, the results of the model show a small tendency to underestimate the experimental distributions for the $c\bar{c}$ dijets. On the other hand, within the same model the $b\bar{b}$-dijet data seems to be slightly overestimated (see Appendix B). This may suggest that within our model the production cross-section ratio $R = \frac{c\bar{c}}{b\bar{b}}$ is not well reproduced.

The conclusion above can be directly examined because the LHCb Collaboration has also presented the corresponding distributions of the ratio $R = \frac{c\bar{c}}{b\bar{b}}$ as functions of the leading jet η, rapidity difference Δy^*, leading jet p_T, and dijet invariant mass $M_{Q\bar{Q}-\text{dijet}}$. A comparison of our predictions to the experimental distributions is shown in Fig. 14. The theoretical ratio is identical for all gluon uPDF models used here. The predicted ratios are slightly above 1 and are almost independent of the considered kinematic variables. The experimental results are slightly larger than

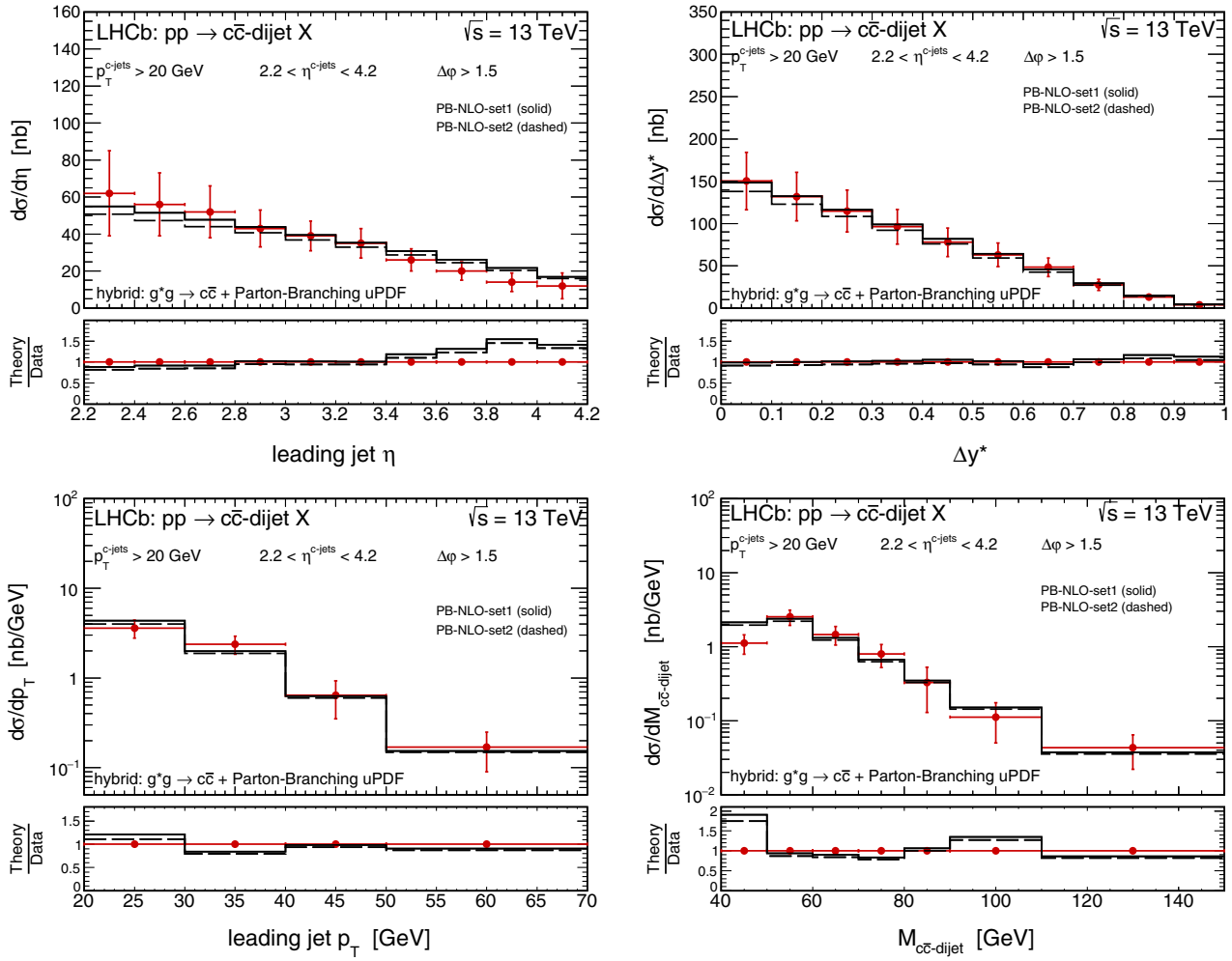

FIG. 12. Same as in Fig. 10 but here the parton-branching uPDFs are used.

the predictions. In general, we obtain an agreement between the theory and the experimental data; however, we reach only the lower experimental limits defined by large total experimental uncertainties. We will continue the discussion of the charm-to-bottom ratio in the following.

F. Comparison with the results of the collinear approach

Finally, we wish to compare our predictions based on the k_T-factorization framework with those obtained according to the collinear approximation. In Figs. 15, 16, and 17 we plot our hybrid model results for the PB-NLO-set1 uPDF (solid bands and histograms) and the results of two different collinear approach calculations: MadGraph5_aMC@NLO [89] (dashed bands) and PYTHIA8 [90] (dotted histograms), both taken from Ref. [46]. The two models correspond to NLO and LO matrix element calculations, respectively, supplemented further with dedicated parton showers.

The main conclusion is that all three models presented here lead to rather consistent results. The PYTHIA8 predictions are very similar to the hybrid model results for both $c\bar{c}$ and $b\bar{b}$ dijets. For the case of $b\bar{b}$ production the MadGraph_aMC@NLO framework also leads to a quite similar results. Here, all three approaches show some small tendency to overshoot the LHCb data. For the $c\bar{c}$ dijets we observe that MadGraph_aMC@NLO leads to a slightly larger cross sections with respect to the other two models, showing some tendency to overshoot the LHCb data within the central prediction. For this model only the lower limit seems to be compatible with both the experimental data and the central predictions of the hybrid model and PYTHIA8. The situation has a direct consequence for the $R = \frac{c\bar{c}}{b\bar{b}}$ distributions. The hybrid model and the PYTHIA8 results give a ratio close to 1, while MadGraph_aMC@NLO leads to slightly larger values, which are preferred by the LHCb data. Definite conclusions here are quite limited because of large theoretical and experimental uncertainties. As was already mentioned the hybrid model and the PYTHIA8 calculations are based on the LO matrix element with real higher-order corrections taken into account by uPDFs or parton showers,

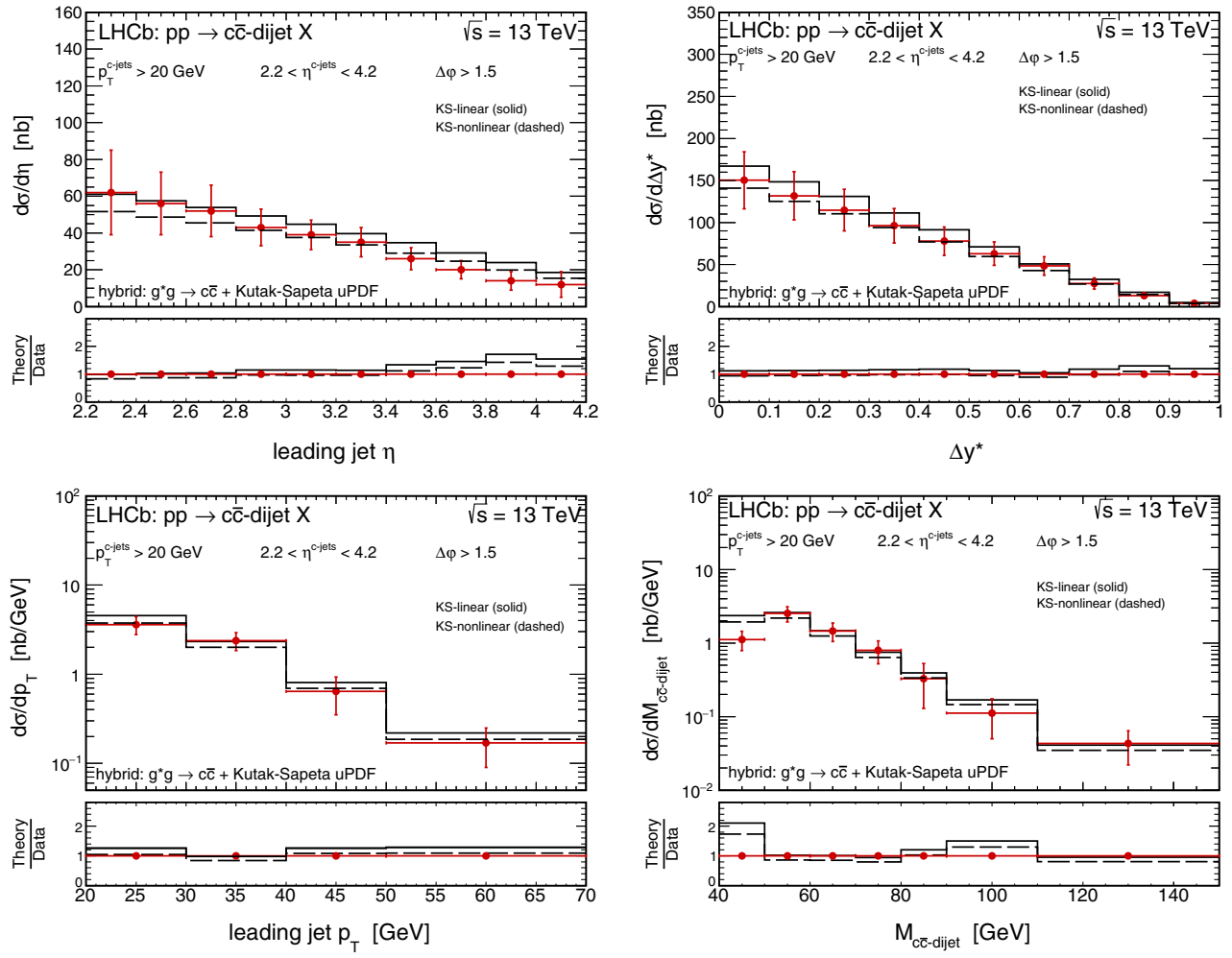

FIG. 13. Same as in Fig. 10 but here the Kutak-Sapeta uPDFs are used.

respectively. Neither include virtual corrections which might be responsible for the observed differences with respect to MadGraph_aMC@NLO. Unfortunately, a full NLO framework within the hybrid (or full) k_T-factorization approach for heavy-quark dijets is quite challenging and still not established.

IV. CONCLUSIONS

In this paper we studied $c\bar{c}$- and $b\bar{b}$-dijet production in pp scattering for $\sqrt{s} = 13$ TeV and LHCb acceptance limitations on jet pseudorapidities $2.2 < \eta_{\mathrm{jet1,2}} < 4.2$, transverse momenta $p_T^{\mathrm{jet1,2}} > 20$ GeV, jet cone $R_{\mathrm{cone}} = 0.5$, and azimuthal angle between the jets $\Delta\varphi > 1.5$. The differential cross sections were calculated within k_T-factorization and hybrid approaches. We used different unintegrated parton distribution functions for the gluon, including the PB, KMR/MRW, and various CCFM models. We calculated distributions in the leading-jet transverse momentum p_T, leading-jet pseudorapidity η, rapidity difference between jets Δy^*, and dijet invariant mass $M_{Q\bar{Q}-\mathrm{dijet}}$. We found that agreement between the predictions and data within the full k_T factorization is strongly related to modeling of the large-x behavior of the gluon uPDFs which is usually not well constrained. For this case, only the PB-NLO-set1 gluon uPDF leads to a satisfactory description of the LHCb data. The rest of the models seem to visibly overestimate the experimental data points. This was understood as being due to the incorrect effective integrated gluon distribution obtained from the unintegrated one for large x.

This problem may be avoided by following the hybrid factorization. Then, a good description of the measured distributions is obtained with the PB-NLO-set1, KMR-MMHT2014nnlo, Kutak-Sapeta, and Jung setA0 CCFM gluon uPDFs for both $c\bar{c}$ and $b\bar{b}$ production taking into account experimental uncertainties. Only the most recent JH-2013-set1 and JH-2013-set2 CCFM gluon uPDFs seem to overestimate the data sets even within the hybrid approach. In any case, we observed a small tendency of

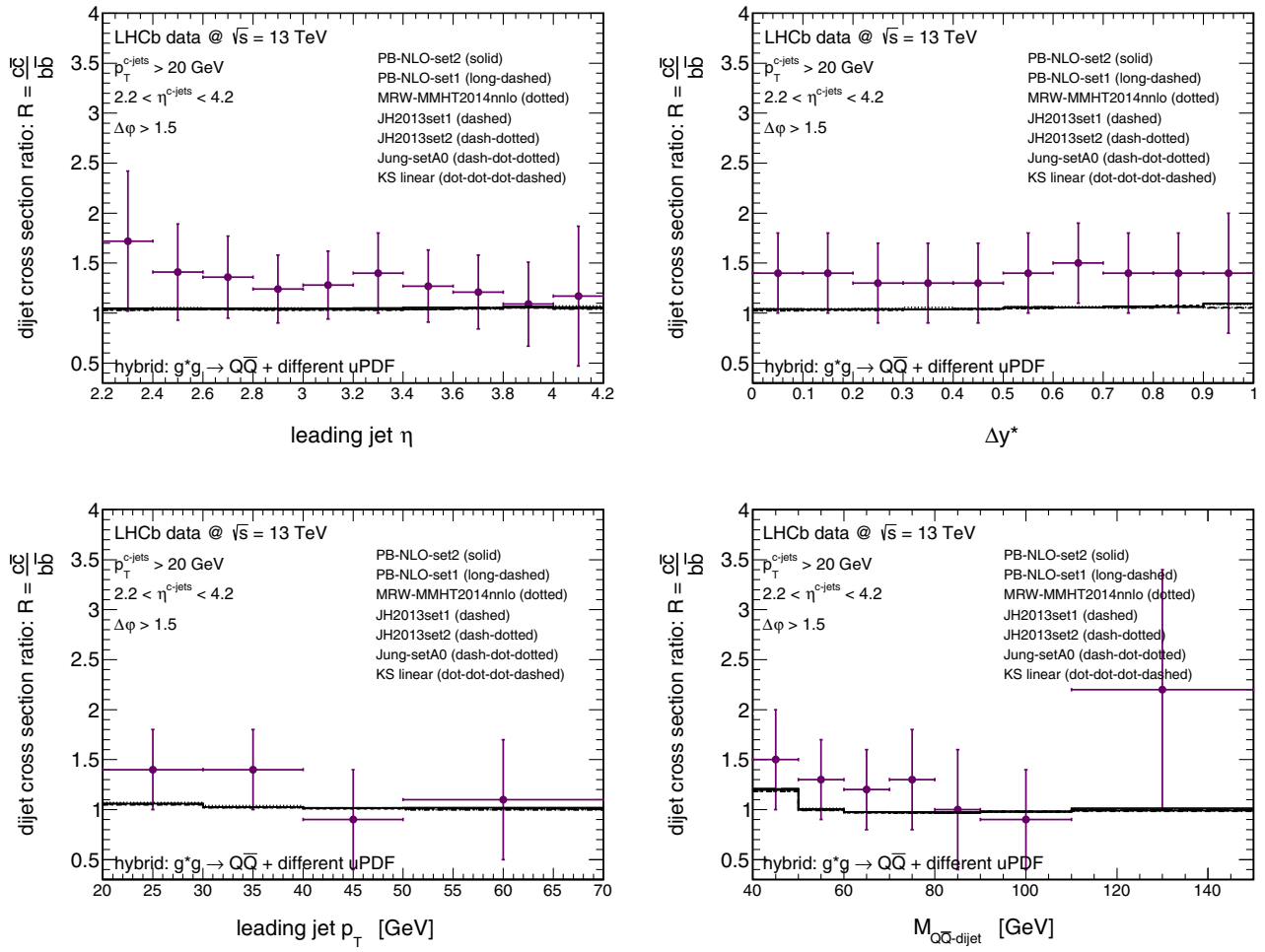

FIG. 14. Ratio $R = \frac{c\bar{c}}{b\bar{b}}$ of the dijet differential cross sections in pp scattering at $\sqrt{s} = 13$ TeV as a function of the leading jet η (top left), rapidity difference Δy^* (top right), leading jet p_T (bottom left), and dijet invariant mass $M_{Q\bar{Q}-\text{dijet}}$ (bottom right). The theoretical histograms correspond to the hybrid model calculations obtained with different gluon uPDFs. Here the default set $\mu^2 = m_T^2$ of the renormalization and factorization scales is used.

our predictions to slightly overestimate the data for $b\bar{b}$ dijets, while the corresponding data for $c\bar{c}$ dijets can be perfectly described within the same gluon uPDFs. In general, taking into account theoretical uncertainties our hybrid model predictions are consistent with collinear results of the PYTHIA8 and MadGraph_aMC@NLO frameworks.

In this paper we performed calculations with different gluon uPDFs. They were constructed using quite different physics arguments as discussed in Sec. II C. The heavy-flavor dijet production is a kind of testbed for them. Some of them can be already eliminated. The main problems of the CCFM gluon uPDFs are related to the large-x region. This is probably due to the fact that they were fitted to deep inelastic scattering data in the region where quark/antiquark contributions should be explicitly included. One of the gluon uPDFs used (Kutak-Sapeta model) includes saturation effects. However, the dijet data are not sensitive to the region of very small x and small scales where the saturation effects could be visible.

We also presented the ratios of $c\bar{c}$ to $b\bar{b}$ cross sections. We get cross-section ratios very close to 1. This can be understood by the fact that for large transverse momenta the effect of the quark mass is rather small. A slightly larger effect, but with large systematic error bars, was obtained in the experimental extraction. In the moment it is difficult to understand the possible disagreement between predictions and the data. In principle, it could be due to inappropriate extraction of $c/\bar{c}$ jets (e.g., by an admixture of light quarks and/or $b/\bar{b}$ jets). We also discussed the effect of damping of the cross section due to a finite jet radius (see Appendix D). It may be expected that statistically a part of the parton (gluon) energy escapes outside of the jet cones. Within this somewhat naive approach one may expect sizable corrections. A much better approach would be to take into account the internal structure of c and b jets due to parton

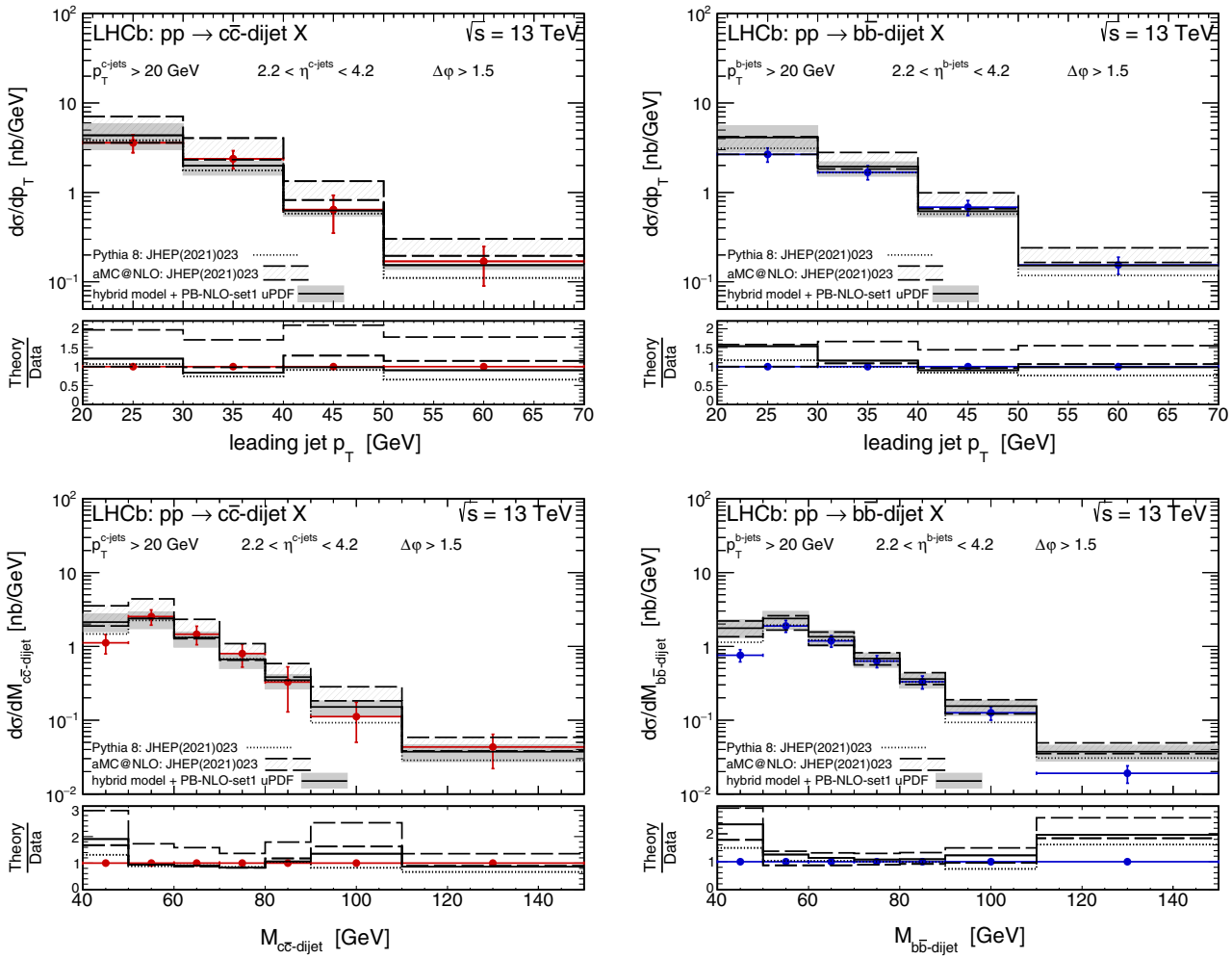

FIG. 15. Differential cross sections for forward production of $c\bar{c}$ (left panels) and $b\bar{b}$ dijets (right panels) in pp scattering at $\sqrt{s} = 13$ TeV as functions of the leading jet p_T (top panels) and dijet invariant mass $M_{Q\bar{Q}-\mathrm{dijet}}$ (bottom panels). Here we compare our predictions of the hybrid model obtained with the PB-NLO-set1 gluon uPDF (solid bands) with two different collinear approach calculations: MadGraph_aMC@NLO (dashed bands) and PYTHIA8 (dotted histograms), both taken from Ref. [46]. More details can be found in the figure.

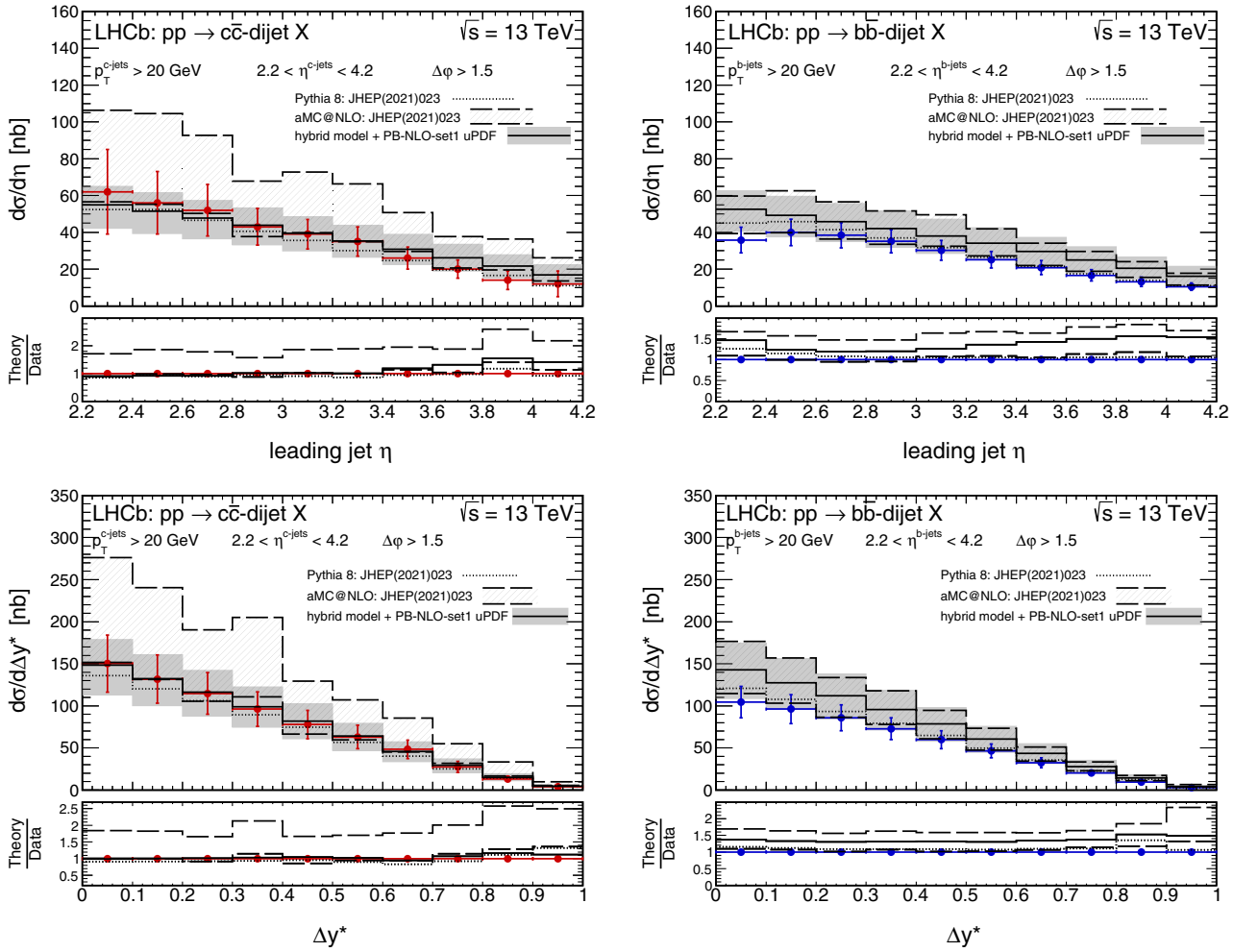

FIG. 16. Same as in Fig. 15 but here the leading jet η (top panels) and rapidity difference Δy^* (bottom panels) distributions are shown.

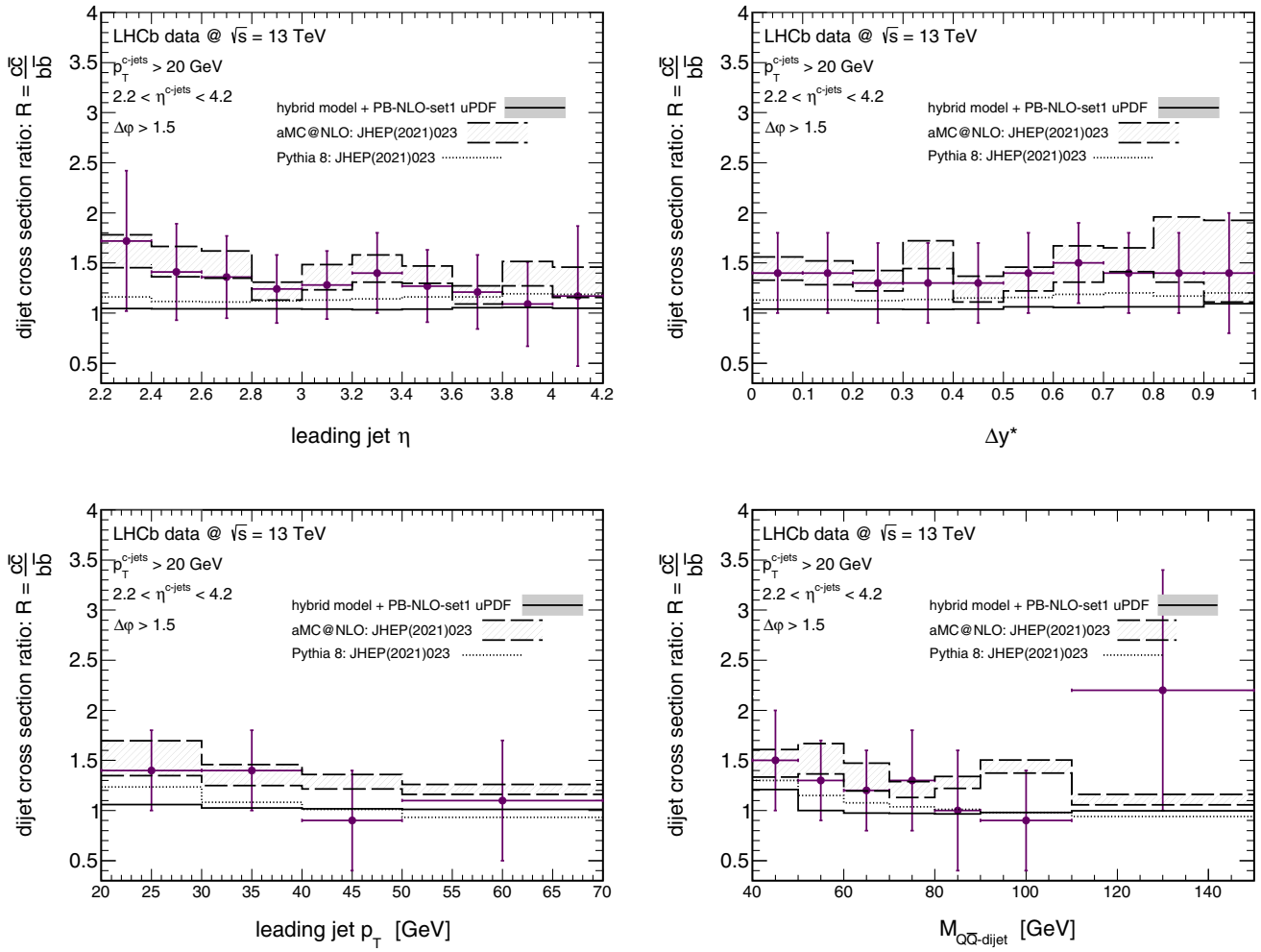

FIG. 17. Ratio $R = \frac{c\bar{c}}{b\bar{b}}$ of the dijet differential cross sections in pp scattering at $\sqrt{s} = 13$ TeV as a function of the leading jet η (top left), rapidity difference Δy^* (top right), leading jet p_T (bottom left), and dijet invariant mass $M_{b\bar{b}-\text{dijet}}$ (bottom right). Here we compare our predictions of the hybrid model obtained with the PB-NLO-set1 gluon uPDF (solid histograms) with two different collinear approach calculations: MadGraph_aMC@NLO (dashed bands) and PYTHIA8 (dotted histograms), both taken from Ref. [46]. More details can be found in the figure.

showers. This definitely goes beyond the scope of the present paper.

In our k_T-factorization approach the production rates for c and $\bar{c}$, as well as for b and $\bar{b}$ are identical (symmetric). Asymmetry effects ($\frac{d\sigma(c)}{d\xi} \neq \frac{d\sigma(\bar{c})}{d\xi}$ and $\frac{d\sigma(b)}{d\xi} \neq \frac{d\sigma(\bar{b})}{d\xi}$, where ξ schematically represents y and p_T) were discussed in Ref. [91]. The asymmetry effects found there are rather small, of the order of 1%. Also, the contribution of electroweak processes (as discussed in Ref. [91]) is rather small, so we think that these interesting effects are not crucial for our studies.

ACKNOWLEDGMENTS

A. S. is indebted to Marcin Kucharczyk for a discussion about jet size and jet definition. This work and the stay of R. M. in Lund was supported by the Bekker Program of the Polish National Agency for Academic Exchange under Contract No. PPN/BEK/2020/1/00187/U/00001. This study was also partially supported by the Polish National Science Center Grant No. UMO-2018/31/B/ST2/03537 and by the Center for Innovation and Transfer of Natural Sciences and Engineering Knowledge in Rzeszów. R. P. is supported in part by the Swedish Research Council Grants, contract No. 621-2013-4287 and No. 2016-05996, as well as by the European Research Council under the European Union's Horizon 2020 research and innovation programme (Grant agreement No. 668679).

APPENDIX A: BOTTOM DIJETS WITHIN THE STANDARD k_T FACTORIZATION

Here we wish to show our results for $b\bar{b}$-dijet production obtained within the standard framework of the

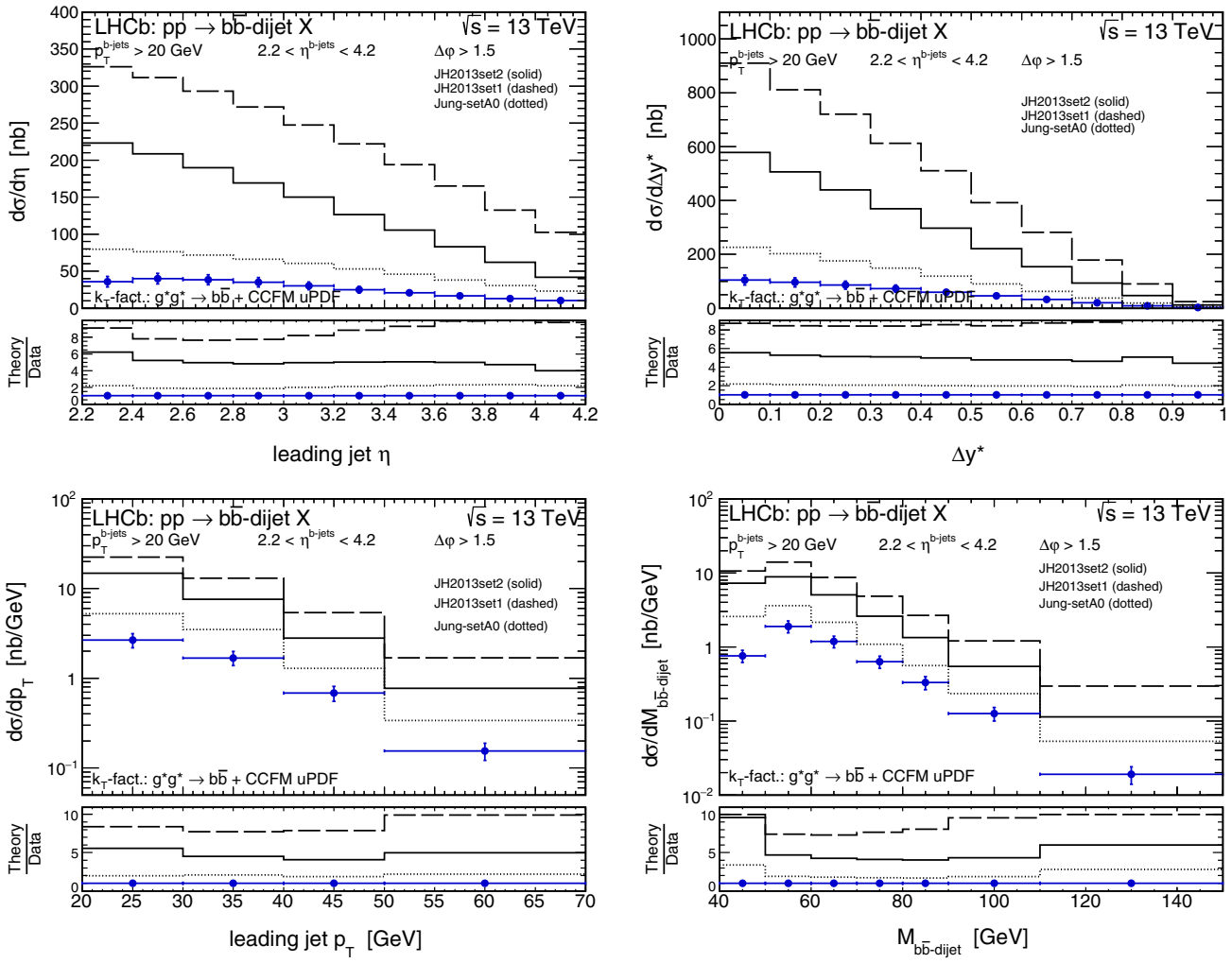

FIG. 18. Differential cross sections for forward production of $b\bar{b}$ dijets in pp scattering at $\sqrt{s} = 13$ TeV as functions of the leading jet η (top left), rapidity difference Δy^* (top right), leading jet p_T (bottom left), and dijet invariant mass $M_{b\bar{b}-\mathrm{dijet}}$ (bottom right). Here the dominant pQCD $g^*g^* \to b\bar{b}$ mechanism is taken into account. The theoretical histograms correspond to the k_T-factorization calculations obtained with the CCFM uPDFs.

k_T-factorization approach. In Figs. 18, 19, and 20, similarly as in the case of charm dijets, we compare our predictions for the CCFM, KMR/MRW, and parton-branching gluon uPDFs to the LHCb experimental data.

Our basic findings about the application of different uPDF models in the description of the LHCb $c\bar{c}$-dijet data also applies here. The main conclusion from a comparison of our predictions with the $b\bar{b}$-dijet data is that the CCFM and MRW/KMR gluon densities lead to a larger discrepancy between predictions and data, overshooting the $b\bar{b}$-dijet data points even more than in the $c\bar{c}$-dijet case. On the other hand, the parton-branching densities describe the bottom data better than the charm data, where a small missing strength is found.

APPENDIX B: BOTTOM DIJETS WITHIN THE HYBRID FACTORIZATION

Here we repeat the analysis performed within the hybrid model for charm dijets, but now we consider the $b\bar{b}$-dijet LHCb data (see Figs. 21–24). As already mentioned, our predictions are almost independent of the heavy-quark mass so the theoretical distributions for bottom quarks are almost identical to those obtained for charm quarks; however, the experimental data points are different. The

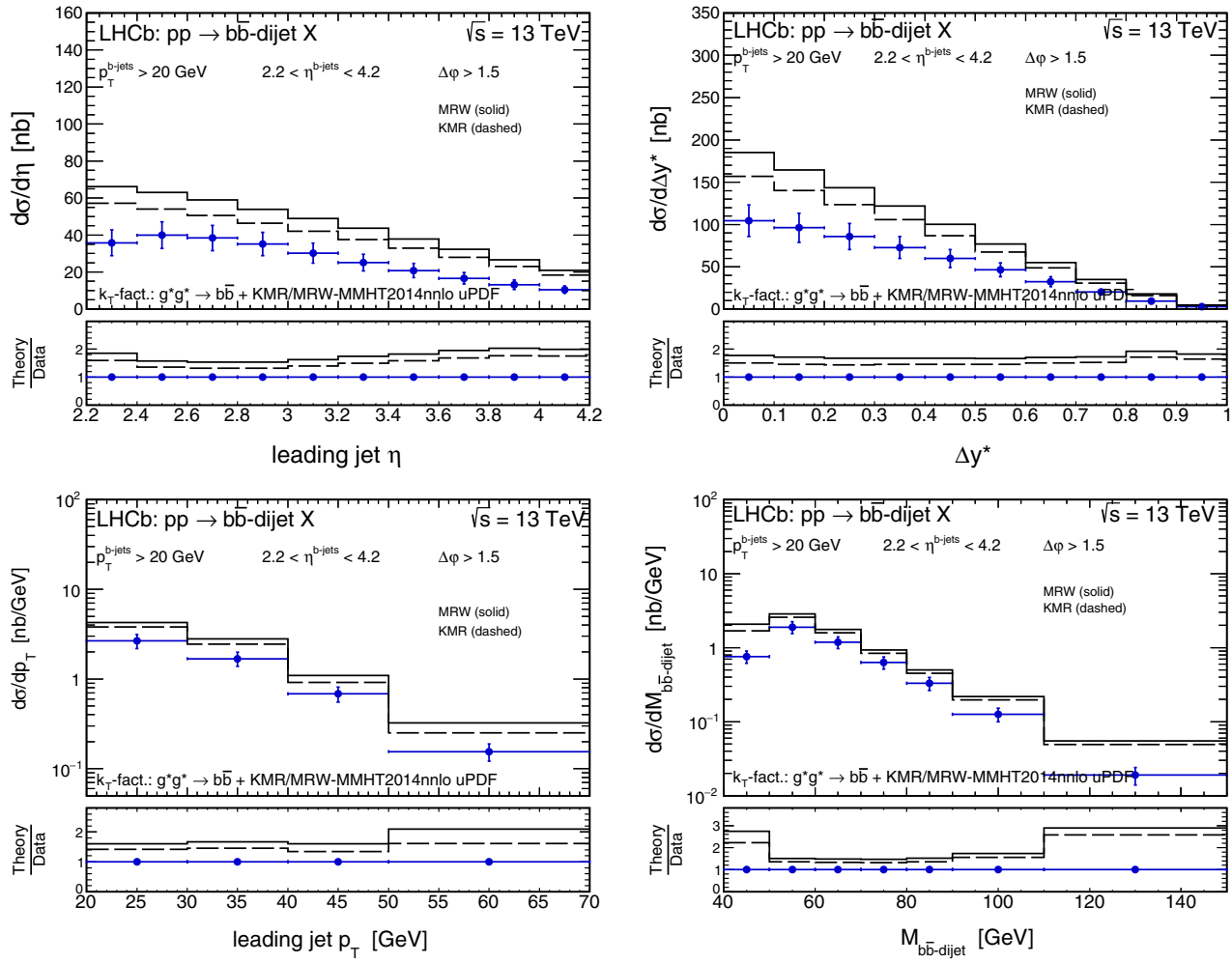

FIG. 19. Same as in Fig. 18 but here the KMR and MRW uPDFs are used.

Jung setA0, KMR, and KS-linear gluon uPDFs provide a very good description of the charm dijet data within the hybrid model, here showing a visible tendency to overshoot the bottom dijet data. Again, the PB-NLO-set1 uPDF leads to the best agreement with the data; however, the theoretical cross section slightly overestimates the experimental point in the very first bin in the leading jet transverse momentum. The discrepancy also affects the leading jet η and rapidity difference Δy^* distributions.

APPENDIX C: SCALE DEPENDENCE OF THE PREDICTIONS

Here we wish to discuss the main uncertainties of our predictions. As we have already shown, an important source of uncertainty in the present study is the modeling of the unintegrated gluon densities in the proton. Here we wish to focus on the second important source of uncertainties, that is, the scale dependence of our predictions.

In Fig. 25 we plot the hybrid model results for the PB-NLO-set1 gluon uPDF, where the shaded bands represent the scale uncertainties calculated by varying the central set of the renormalization and factorization scales up and down independently by a factor of 2. Here the central set of the scales corresponds to the $\mu^2 = m_t^2$ case. As we can see, the sensitivity is sizable but not huge and seems to decrease with the leading jet transverse momentum.

In Fig. 26 we present how our results depend on the definition of the central set for the scales. The sensitivity has a similar size as above and one has to keep in mind that different choices of the central sets might slightly modify the overall picture. In principle, taking $\mu^2 = M^2_{Q\bar{Q}}$ we get slightly smaller cross sections which means that within this choice we get better agreement with the data for bottom

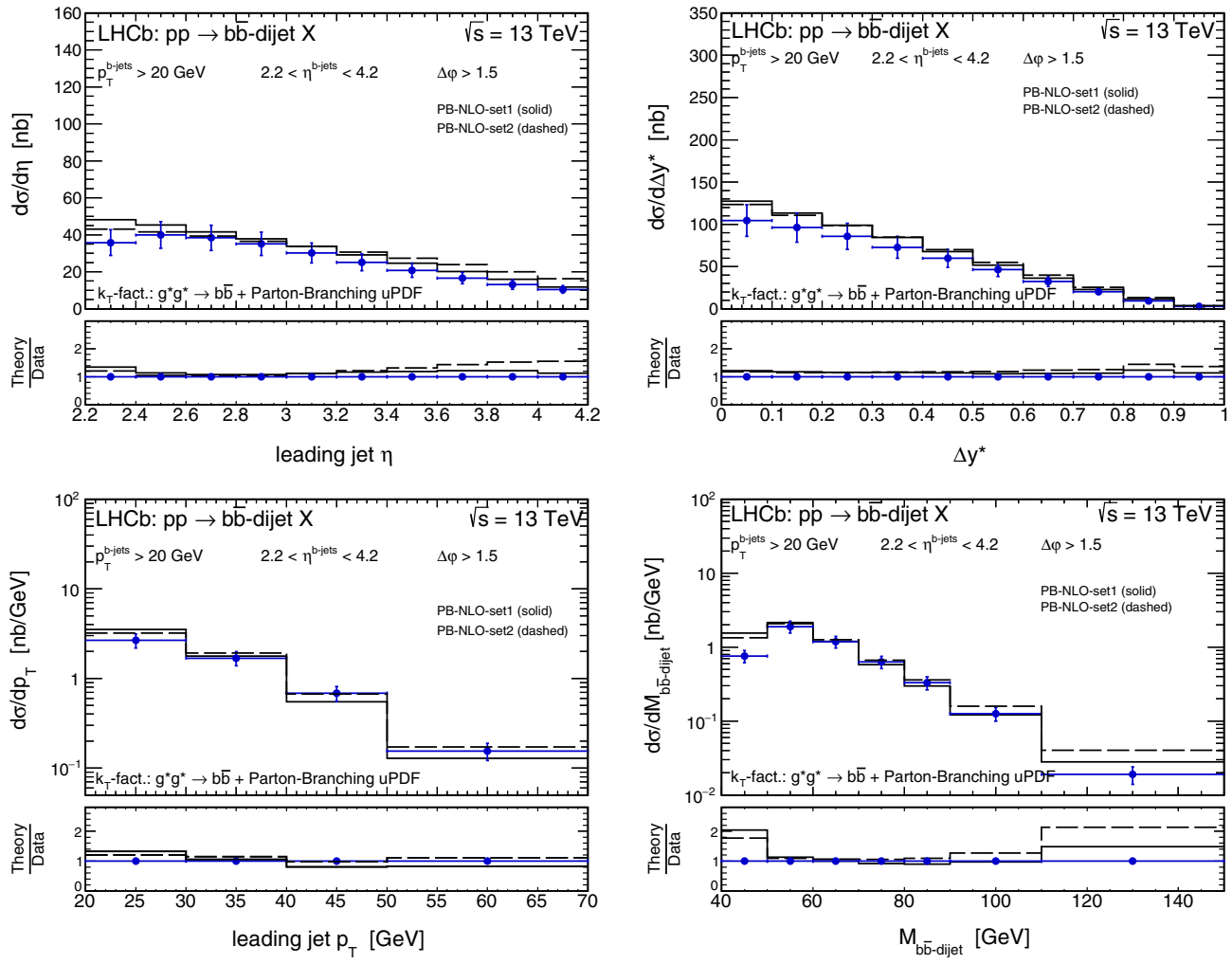

FIG. 20. Same as in Fig. 18 but here the parton-branching uPDFs are used.

than for charm production—in opposite to conclusions obtained with our default scale set.

What we find interesting here is that playing with the definition of the central scale does not improve our description of the charm-to-bottom production cross section ratios (see Fig. 27).

APPENDIX D: COMMENT ON FINITE JET SIZE EFFECTS

So far we have calculated distributions at the parton level. The agreement with experimental data, however, is quite good for both $c\bar{c}$ and $b\bar{b}$ dijets. In principle, one could worry about jet-size effects. The LHCb Collaboration chose the jet cone size $R_{\rm cone} = 0.5$ in their analysis [46]. Could this affect our partonic results?

In general, a thorough answer to this question requires modeling of c and b jets which is rather complicated and goes beyond the scope of the present paper. Instead of following this path, we will try to estimate the effect approximately, as was done for one jet case in Ref. [92].

It is the energy of the jet that determines the shape of the jet [92]. The larger the energy of the jet, the smaller the finite cone size effects. In Fig. 28 we show double differential cross sections, probed in the LHCb kinematics, as functions of the energies of both jets.

Typical jet energies are relatively large, $E_1, E_2 > 100$ GeV. In the approach of Ref. [92] the basic ingredient

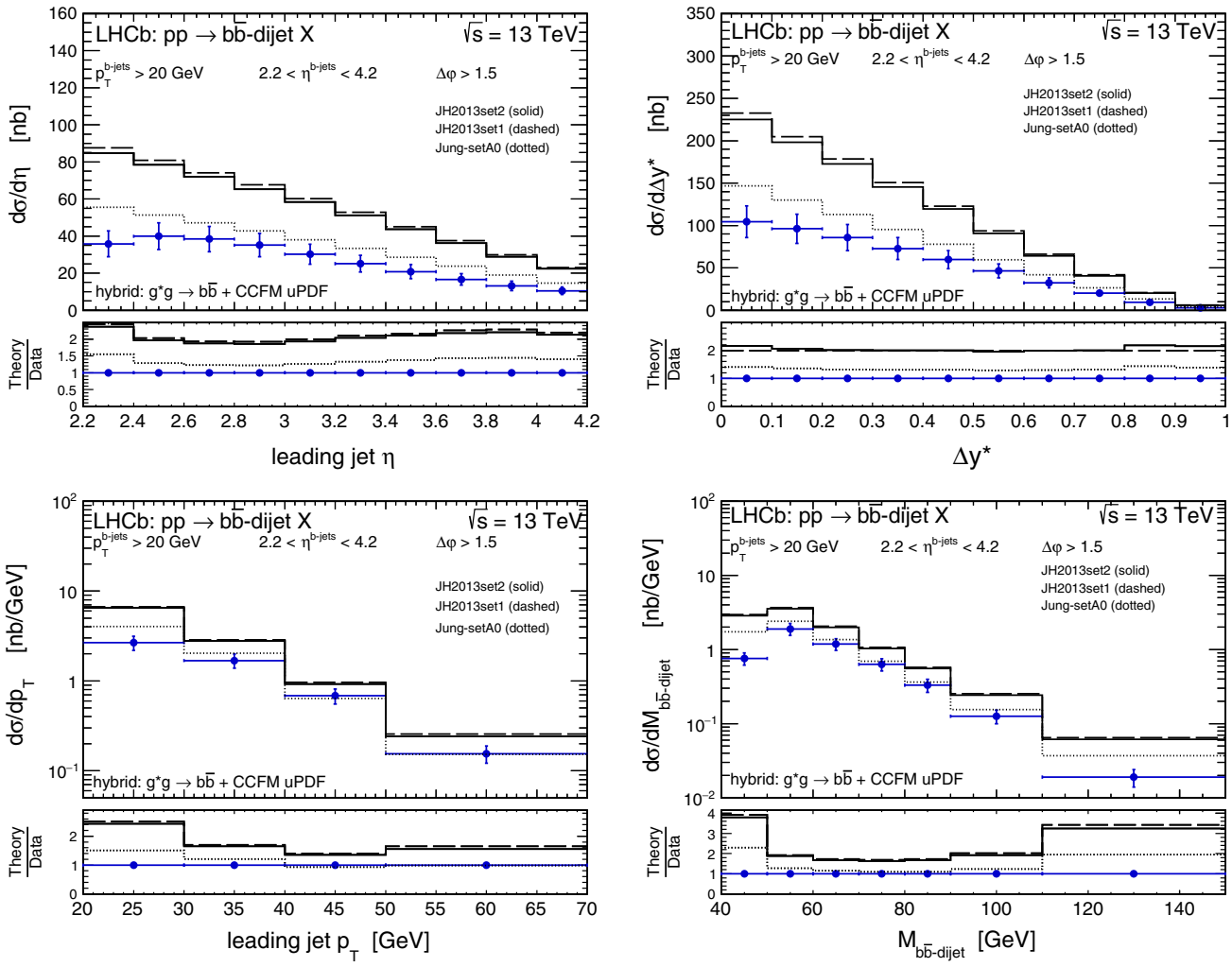

FIG. 21. Differential cross sections for forward production of $b\bar{b}$ dijets in pp scattering at $\sqrt{s} = 13$ TeV as functions of the leading jet η (top left), rapidity difference Δy^* (top right), leading jet p_T (bottom left), and dijet invariant mass $M_{b\bar{b}-\text{dijet}}$ (bottom right). Here the dominant pQCD $g^*g \to b\bar{b}$ mechanism is taken into account. The theoretical histograms correspond to the hybrid model calculations obtained with the CCFM uPDFs.

is $dE_g/dxdk^2$, where E_g is the energy of the emitted gluon, x is its longitudinal momentum fraction, and k^2 is the transverse momentum squared of the gluon with respect to the heavy quark (c or b in our case). This quantity depends on the mass of the emitting quark. In principle, one can expect a spectacular effect known as "dead cone" [93]. The dead cone effect was recently observed experimentally for the first time by the ALICE Collaboration [94]. Energy loss due to emission outside of the jet cone can then be written as

$$\Delta E_g = \int \frac{dE_g}{dxdk^2}\theta(\theta > \theta_{\text{open}}(R_{\text{cone}})), \qquad \text{(D1)}$$

where $\theta_{\text{open}}(R_{\text{cone}})$ is the jet opening angle corresponding to a given jet radius R_{cone}. The distribution $\frac{dE_g}{dxdk^2}$ is obtained [92] from a generalization of the Gunion-Bertsch formula [95] for the gluon number distribution $\frac{dn_g}{dxdk^2}$.

At high energies, as in our case, such effects are completely unimportant as the dead cone angle is of the order of a small fraction of one degree. In our case, it is the energy (transverse momentum) that escapes from experimentally defined jet cones. We estimate that in our case the relative energy loss $\Delta E/E$, including the range of jet energies and $R_{\text{cone}} = 0.5$, is of the order of a few percent. It is reasonable to expect that the same is true for $\Delta p_T/p_T$. The main effect is due to the fact that the cuts are imposed on the measured transverse momenta, not the momenta of heavy quarks/antiquarks, which are of course bigger than the measured ones. In our case we have to apply this procedure to both measured jets. This leads to a damping of the cross section by approximately a few percent. We have checked

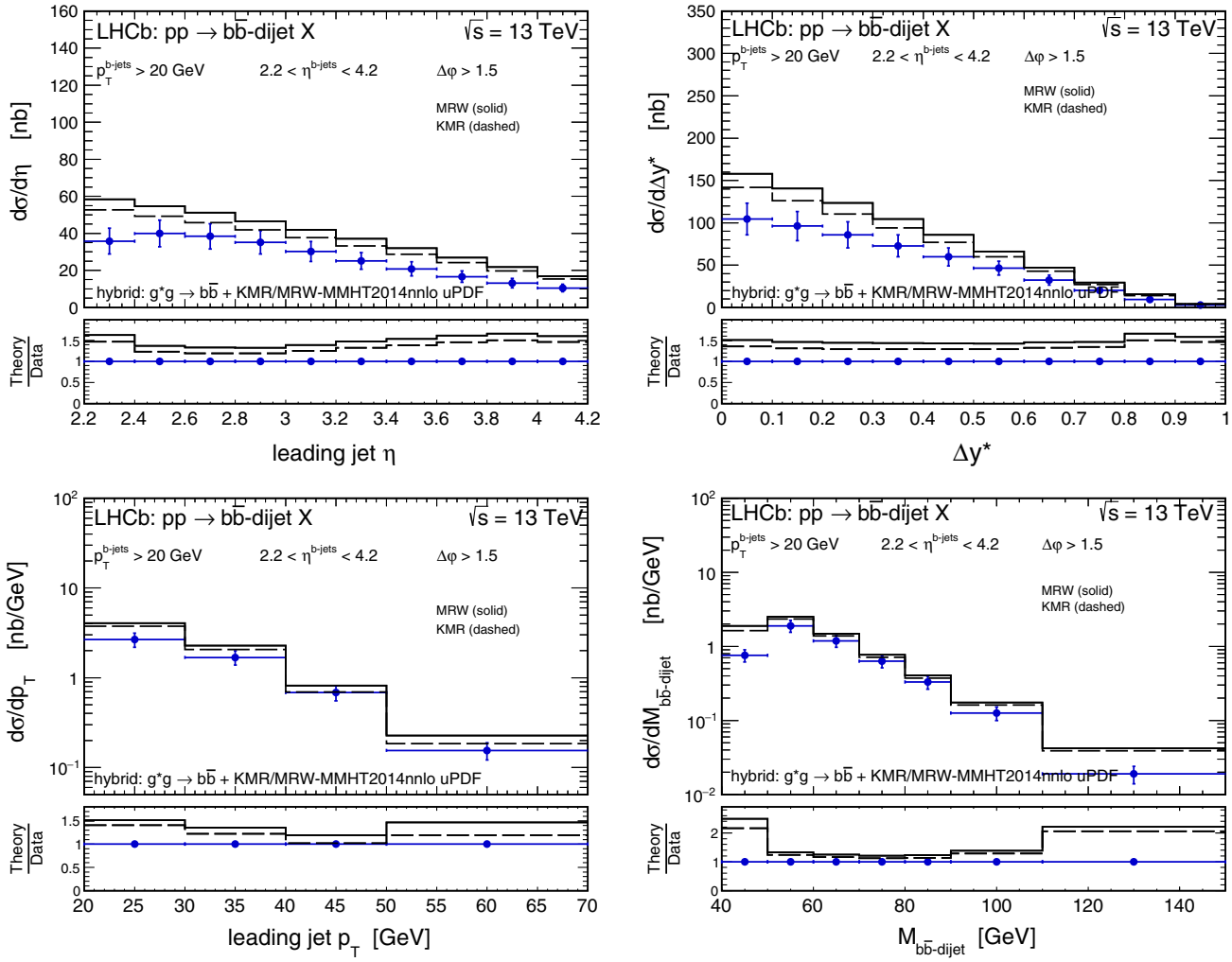

FIG. 22. Same as in Fig. 21 but here the KMR and MRW uPDFs are used.

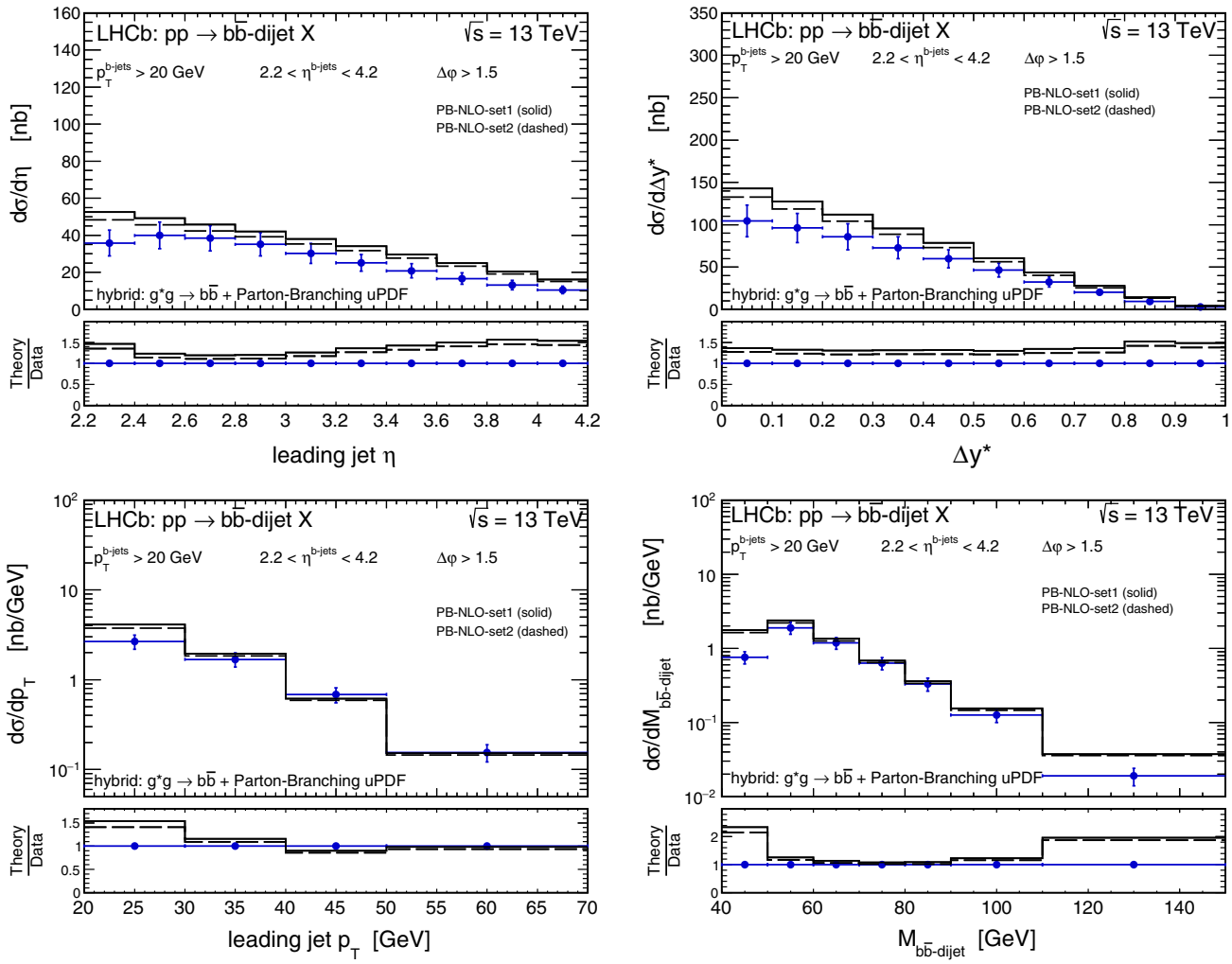

FIG. 23. Same as in Fig. 21 but here the parton-branching uPDFs are used.

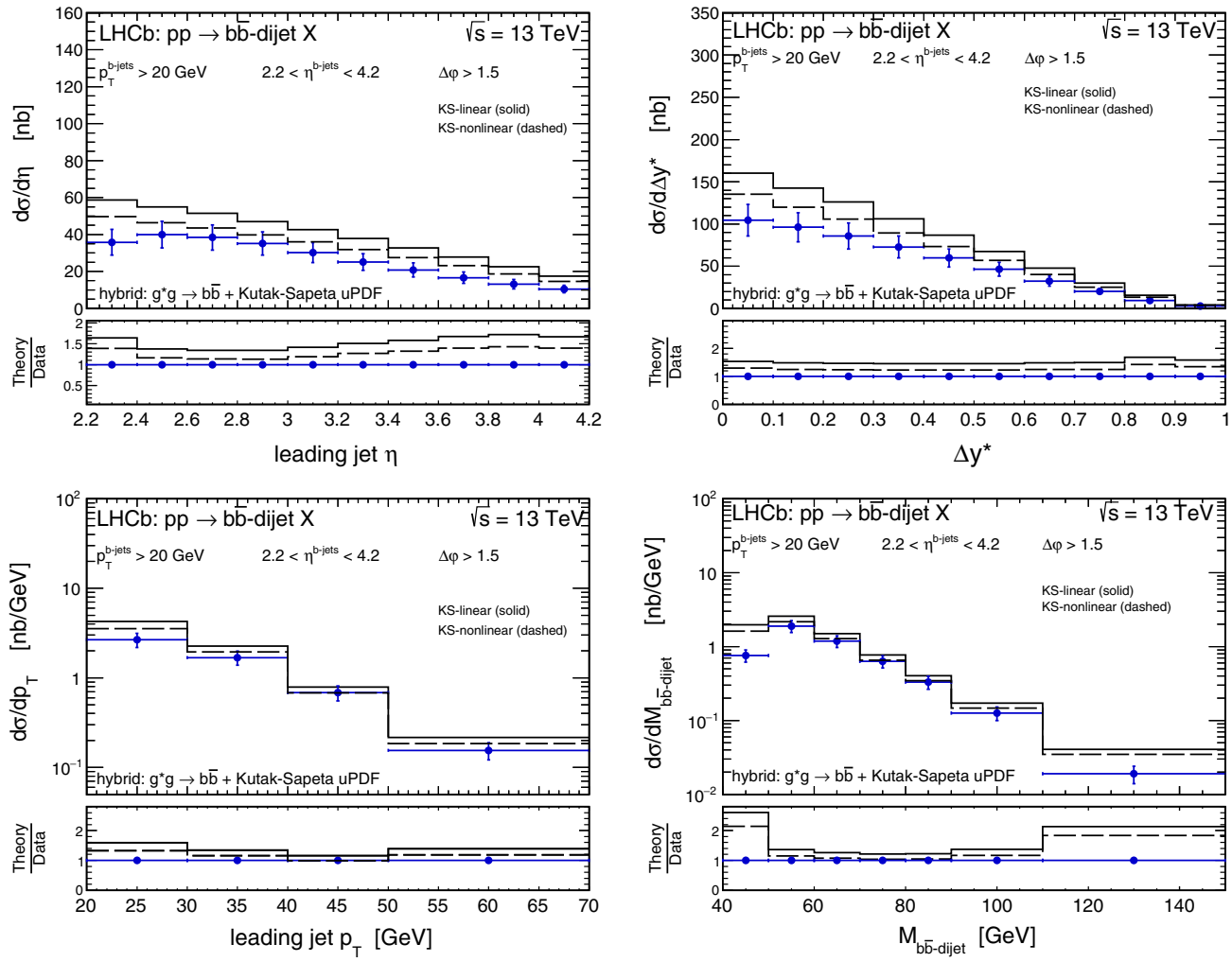

FIG. 24. Same as in Fig. 21 but here the Kutak-Sapeta uPDFs are used.

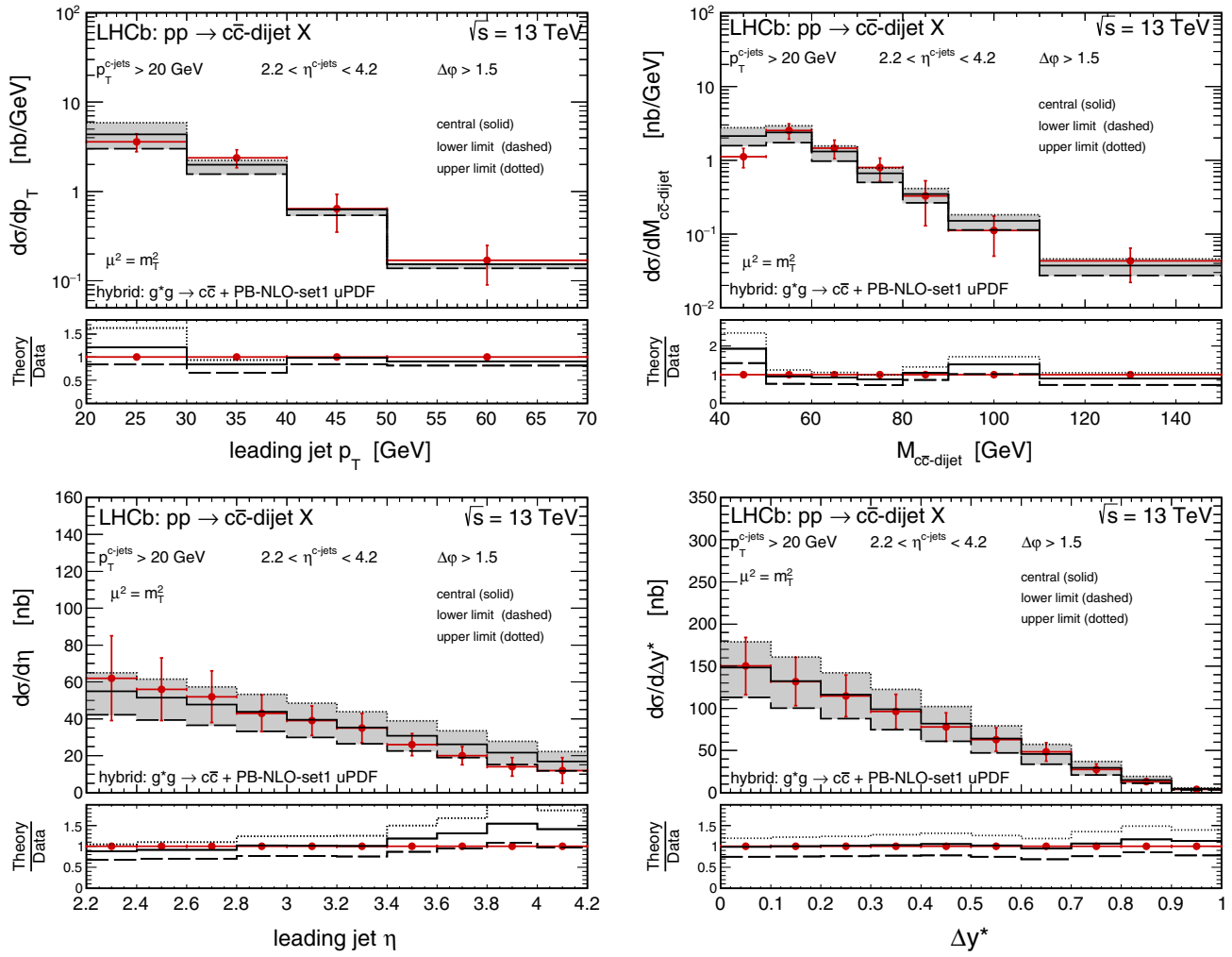

FIG. 25. Differential cross sections for forward production of $c\bar{c}$ (left panels) and $b\bar{b}$ dijets (right panels) in pp scattering at $\sqrt{s} = 13$ TeV as functions of the leading jet p_T (top left panel), dijet invariant mass $M_{Q\bar{Q}-\mathrm{dijet}}$ (top right panel), leading jet η (bottom left panel), and rapidity difference Δy^* (bottom right panel). The shaded bands represent the scale uncertainties calculated by varying the central set of the renormalization and factorization scales up and down independently by a factor of 2. Here the hybrid model with the PB-NLO-set1 gluon uPDF is used.

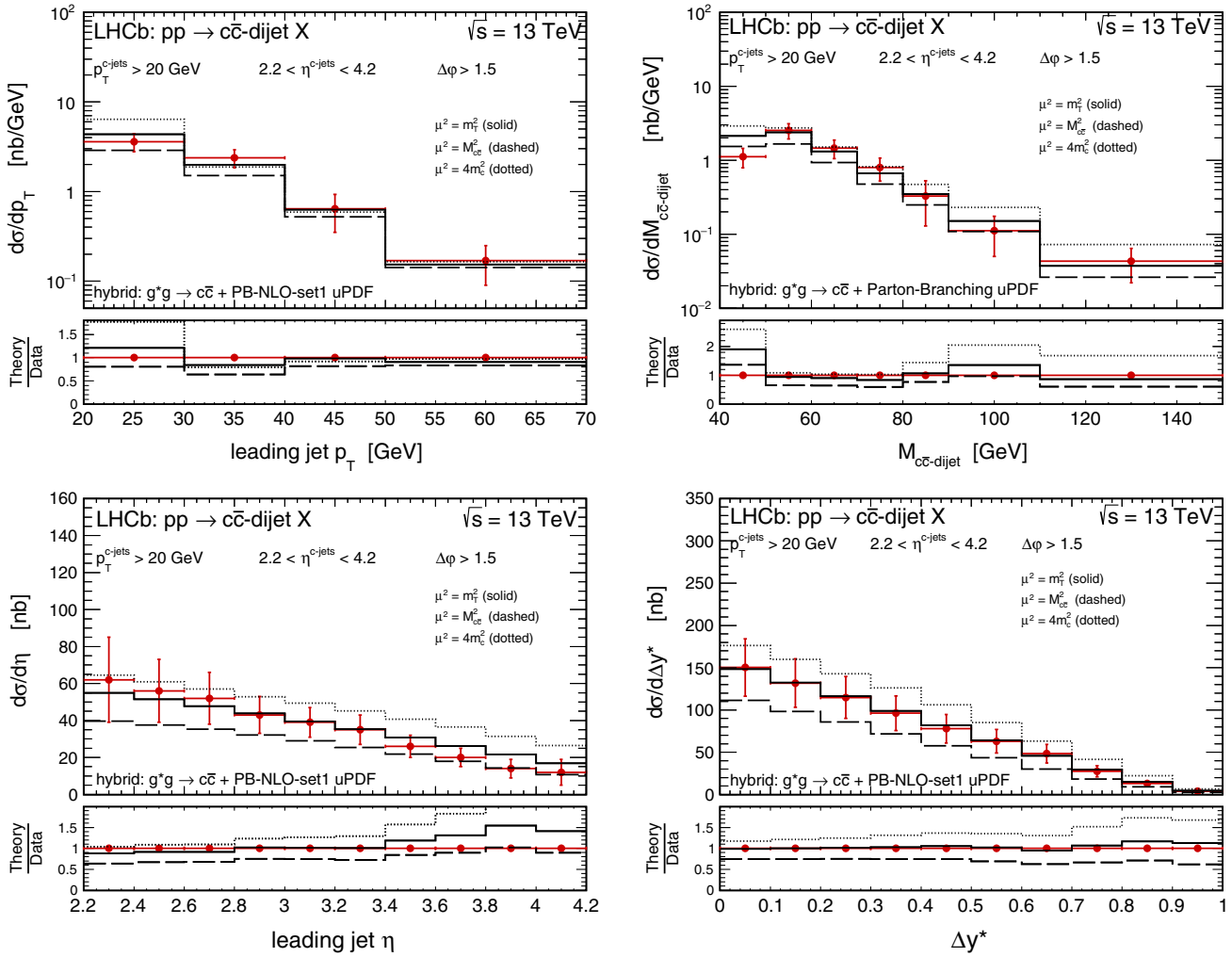

FIG. 26. Differential cross sections for forward production of $c\bar{c}$- (left panels) and $b\bar{b}$ dijets (right panels) in pp scattering at $\sqrt{s} = 13$ TeV as functions of the leading jet p_T (top left panel), dijet invariant mass $M_{Q\bar{Q}-\mathrm{dijet}}$ (top right panel), leading jet η (bottom left panel), and rapidity difference Δy^* (bottom right panel). The three different lines correspond to the different choices for the central set of the renormalization and factorization scales. More details can be found in the figure. Here the hybrid model with the PB-NLO-set1 gluon uPDF is used.

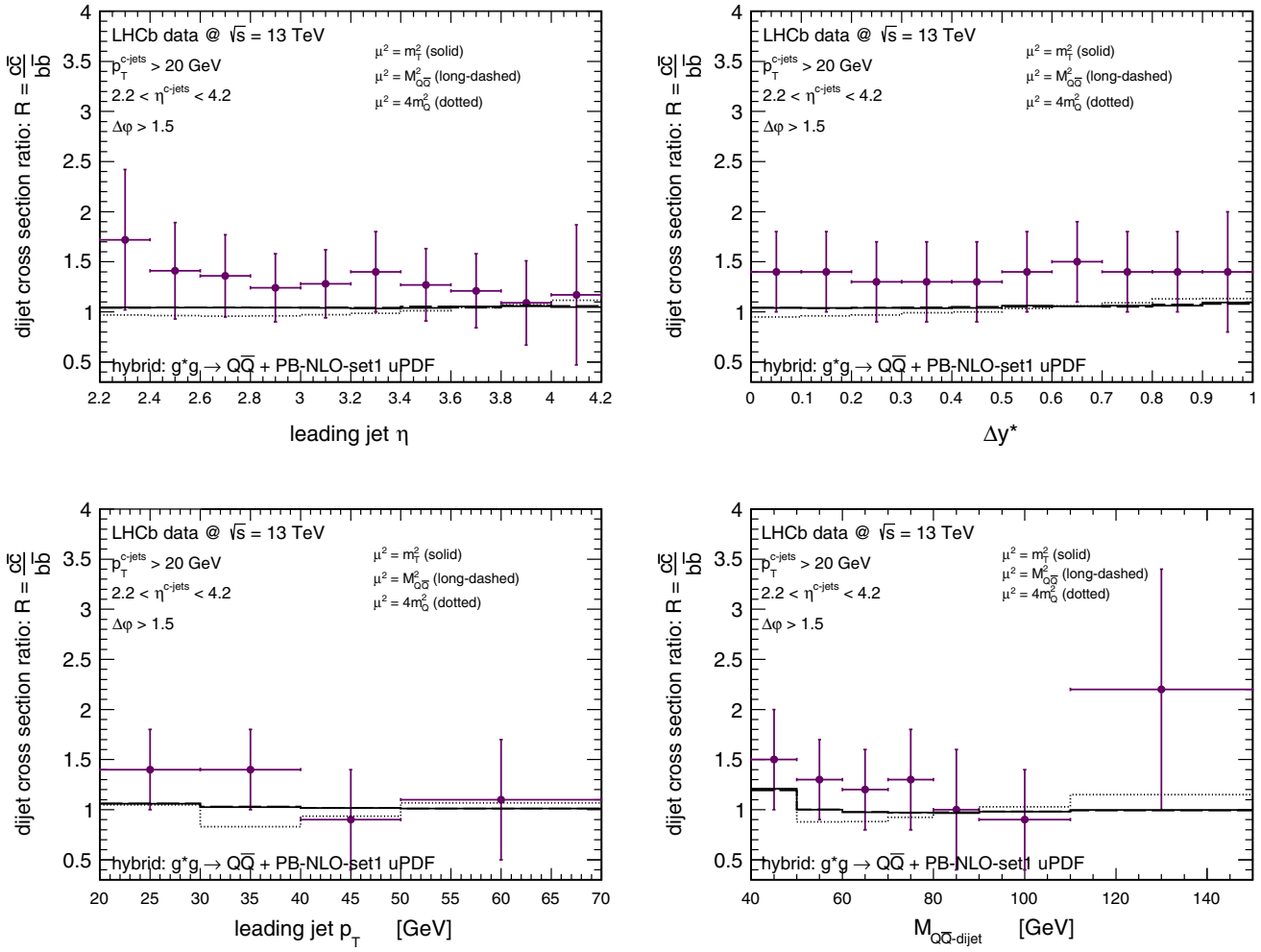

FIG. 27. Same as in Fig. 14 but here the three different lines correspond to the different choices for the central set of the renormalization and factorization scale variables. More details can be found in the figure. Here the hybrid model with the PB-NLO-set1 gluon uPDF is used.

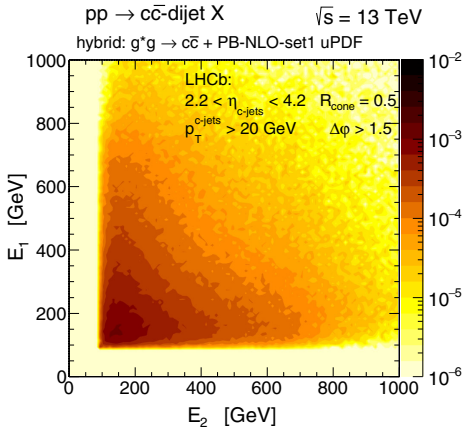

FIG. 28. Double differential cross sections in energies of both jets for forward production of $c\bar{c}$ dijets in pp scattering at $\sqrt{s} =$ 13 TeV probed in the LHCb experiment [46] as functions of the energies of both jets.

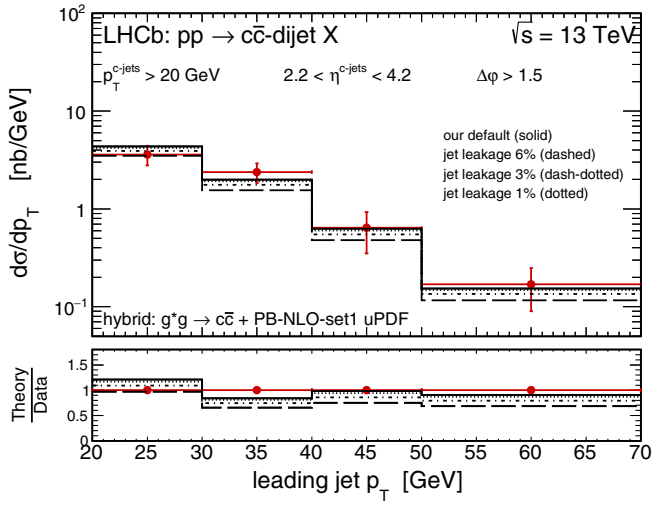

FIG. 29. Differential cross sections for forward production of $c\bar{c}$ dijets in pp scattering at $\sqrt{s} = 13$ TeV as functions of the leading jet p_T for three different values of the jet leakage effect.

that the damping is practically the same for $c/\bar{c}$ and $b/\bar{b}$ quarks/antiquarks. In our energy range the quark-mass effect is negligible. We conclude that jet cone size effects are probably not responsible for the charm-to-bottom ratios discussed in our paper. We think that the effect of the shape of the heavy-quark jets requires further studies, not only in the context of this study.

In Fig. 29 we show results for different (independent of transverse momentum and pseudorapidity) values of the leakage of the energy outside of the jet cone radius $R_{\rm cone} = 0.5$. Here we assume in addition that $\frac{\Delta p_T}{p_T} \approx \frac{\Delta E}{E}$ for both jets. Although the assumed leakage (1%, 3%, 6%) is rather small, the resulting effect on the cross section normalization is sizable.

[1] B. Abelev *et al.* (ALICE Collaboration), J. High Energy Phys. 01 (2012) 128.
[2] B. Abelev *et al.* (ALICE Collaboration), Phys. Lett. B **718**, 279 (2012).
[3] B. Abelev *et al.* (ALICE Collaboration), J. High Energy Phys. 07 (2012) 191.
[4] S. Acharya *et al.* (ALICE Collaboration), Eur. Phys. J. C **79**, 388 (2019).
[5] G. Aad *et al.* (ATLAS Collaboration), Nucl. Phys. **B907**, 717 (2016).
[6] CMS Collaboration, Report No. CMS-PAS-HIN-16-001.
[7] R. Aaij *et al.* (LHCb Collaboration), Nucl. Phys. **B871**, 1 (2013).
[8] R. Aaij *et al.* (LHCb Collaboration), J. High Energy Phys. 03 (2016) 159; 09 (2016) 13; 05 (2017) 74.
[9] ATLAS Collaboration, Report No. ATLAS-CONF-2013-008.
[10] S. Chatrchyan *et al.* (CMS Collaboration), Phys. Rev. Lett. **106**, 252001 (2011).
[11] V. Khachatryan *et al.* (CMS Collaboration), Phys. Rev. Lett. **106**, 112001 (2011).
[12] B. Andersson, G. Gustafson, G. Ingelman, and T. Sjostrand, Phys. Rep. **97**, 31 (1983).
[13] B. R. Webber, Nucl. Phys. **B238**, 492 (1984).
[14] R. Maciuła and A. Szczurek, J. Phys. G **47**, 035001 (2020).
[15] A. Szczurek, J. Phys. G **48**, 055010 (2021).
[16] M. Cacciari, S. Frixione, N. Houdeau, M. L. Mangano, P. Nason, and G. Ridolfi, J. High Energy Phys. 10 (2012) 137.
[17] B. A. Kniehl, G. Kramer, I. Schienbein, and H. Spiesberger, Eur. Phys. J. C **72**, 2082 (2012).
[18] M. Klasen, C. Klein-Bösing, K. Kovarik, G. Kramer, M. Topp, and J. Wessels, J. High Energy Phys. 08 (2014) 109.
[19] A. Bhattacharya, R. Enberg, Y. S. Jeong, C. S. Kim, M. H. Reno, I. Sarcevic, and A. Stasto, J. High Energy Phys. 11 (2016) 167.
[20] M. V. Garzelli, S. Alekhin, M. Benzke, B. Kniehl, S. O. Moch, and O. Zenaiev, Proc. Sci. RADCOR2019 (**2019**) 048.
[21] R. Maciuła and A. Szczurek, Phys. Rev. D **87**, 094022 (2013).
[22] R. Maciuła and A. Szczurek, Phys. Rev. D **100**, 054001 (2019).
[23] R. Maciuła, Phys. Rev. D **102**, 014028 (2020).
[24] R. Maciuła and A. Szczurek, Phys. Rev. D **105**, 014001 (2022).
[25] H. Jung, M. Kraemer, A. V. Lipatov, and N. P. Zotov, Phys. Rev. D **85**, 034035 (2012).
[26] A. Karpishkov, V. Saleev, and A. Shipilova, Phys. Rev. D **94**, 114012 (2016).
[27] B. Guiot and A. van Hameren, Phys. Rev. D **104**, 094038 (2021).
[28] V. P. Goncalves, B. Kopeliovich, J. Nemchik, R. Pasechnik, and I. Potashnikova, Phys. Rev. D **96**, 014010 (2017).
[29] R. Aaij *et al.* (LHCb Collaboration), J. High Energy Phys. 06 (2012) 141.
[30] V. Khachatryan *et al.* (CMS Collaboration), J. High Energy Phys. 03 (2011) 136.
[31] R. Maciuła and A. Szczurek, Phys. Rev. D **87**, 074039 (2013).
[32] A. V. Karpishkov, M. A. Nefedov, and V. A. Saleev, Phys. Rev. D **96**, 096019 (2017).
[33] R. Vogt, Phys. Rev. C **98**, 034907 (2018).
[34] D. Souza and N. H. Brook, J. Phys. G **43**, 015001 (2016).
[35] G. Aad *et al.* (ATLAS Collaboration), Eur. Phys. J. C **71**, 1846 (2011).
[36] S. Chatrchyan *et al.* (CMS Collaboration), J. High Energy Phys. 04 (2012) 084.
[37] S. Acharya *et al.* (ALICE Collaboration), J. High Energy Phys. 01 (2022) 178.
[38] A. M. Sirunyan *et al.* (CMS Collaboration), J. High Energy Phys. 05 (2021) 054.
[39] M. Aaboud *et al.* (ATLAS Collaboration), Eur. Phys. J. C **76**, 670 (2016).
[40] A. M. Sirunyan *et al.* (CMS Collaboration), J. High Energy Phys. 03 (2018) 181.
[41] CMS Collaboration, J. Instrum. **17**, P03014 (2022).
[42] A. M. Sirunyan *et al.* (CMS Collaboration), Phys. Lett. B **772**, 306 (2017).
[43] S. Acharya *et al.* (ALICE Collaboration), J. High Energy Phys. 08 (2019) 133.
[44] R. Aaij *et al.* (LHCb Collaboration), J. Instrum. **10**, P06013 (2015).
[45] R. Aaij *et al.* (LHCb Collaboration), J. Instrum. **17**, P02028 (2022).
[46] R. Aaij *et al.* (LHCb Collaboration), J. High Energy Phys. 02 (2021) 023.
[47] L. A. Anchordoqui, A. Ariga, T. Ariga, W. Bai, K. Balazs, B. Batell, J. Boyd, J. Bramante, M. Campanelli, and A. Carmona *et al.*, Phys. Rep. **968**, 1 (2022).

[48] S. Catani, M. Ciafaloni, and F. Hautmann, Phys. Lett. B **242**, 97 (1990); Nucl. Phys. **B366**, 135 (1991); Phys. Lett. B **307**, 147 (1993); J. C. Collins and R. K. Ellis, Nucl. Phys. **B360**, 3 (1991); L. V. Gribov, E. M. Levin, and M. G. Ryskin, Phys. Rep. **100**, 1 (1983); E. M. Levin, M. G. Ryskin, Yu. M. Shabelsky, and A. G. Shuvaev, Sov. J. Nucl. Phys. **53**, 657 (1991).

[49] M. A. Nefedov, V. A. Saleev, and A. V. Shipilova, Phys. Rev. D **87**, 094030 (2013).

[50] M. A. Nefedov, N. N. Nikolaev, and V. A. Saleev, Phys. Rev. D **87**, 014022 (2013).

[51] R. Maciuła and A. Szczurek, Phys. Rev. D **94**, 114037 (2016).

[52] R. Maciuła and A. Szczurek, Phys. Rev. D **96**, 074013 (2017).

[53] V. A. Bednyakov, S. J. Brodsky, A. V. Lipatov, G. I. Lykasov, M. A. Malyshev, J. Smiesko, and S. Tokar, Eur. Phys. J. C **79**, 92 (2019).

[54] A. V. Lipatov, G. I. Lykasov, M. A. Malyshev, A. A. Prokhorov, and S. M. Turchikhin, Phys. Rev. D **97**, 114019 (2018).

[55] K. Kutak, R. Maciula, M. Serino, A. Szczurek, and A. van Hameren, J. High Energy Phys. 04 (2016) 175.

[56] A. van Hameren, R. Maciuła, and A. Szczurek, Phys. Lett. B **748**, 167 (2015).

[57] M. Nefedov and V. Saleev, Phys. Rev. D **92**, 094033 (2015).

[58] M. Nefedov and V. Saleev, arXiv:1608.04201.

[59] A. van Hameren (private communication).

[60] H. Jung *et al.*, Eur. Phys. J. C **70**, 1237 (2010).

[61] M. Deak, F. Hautmann, H. Jung, and K. Kutak, J. High Energy Phys. 09 (2009) 121.

[62] K. Kutak and S. Sapeta, Phys. Rev. D **86**, 094043 (2012).

[63] P. Kotko, K. Kutak, C. Marquet, E. Petreska, S. Sapeta, and A. van Hameren, J. High Energy Phys. 09 (2015) 106.

[64] M. Ciafaloni, Nucl. Phys. **B296**, 49 (1988); S. Catani, F. Fiorani, and G. Marchesini, Phys. Lett. B **234**, 339 (1990); Nucl. Phys. **B336**, 18 (1990); G. Marchesini, Nucl. Phys. **B445**, 49 (1995).

[65] F. Hautmann, H. Jung, and S. T. Monfared, Eur. Phys. J. C **74**, 3082 (2014).

[66] H. Jung, M. Kraemer, A. V. Lipatov, and N. P. Zotov, J. High Energy Phys. 01 (2011) 085.

[67] F. Hautmann, H. Jung, A. Lelek, V. Radescu, and R. Zlebcik, J. High Energy Phys. 01 (2018) 070.

[68] A. Bermudez Martinez, P. Connor, H. Jung, A. Lelek, R. Žlebčík, F. Hautmann, and V. Radescu, Phys. Rev. D **99**, 074008 (2019).

[69] S. T. Monfared, F. Hautmann, H. Jung, and M. Schmitz, Proc. Sci. DIS2019 (**2019**) 136. [arXiv:1908.01621].

[70] F. Hautmann, H. Jung, M. Krämer, P. Mulders, E. Nocera, T. Rogers, and A. Signori, Eur. Phys. J. C **74**, 3220 (2014).

[71] M. Kimber, A. D. Martin, and M. Ryskin, Eur. Phys. J. C **12**, 655 (2000).

[72] M. Kimber, A. D. Martin, and M. Ryskin, Phys. Rev. D **63**, 114027 (2001).

[73] G. Watt, A. Martin, and M. Ryskin, Eur. Phys. J. C **31**, 73 (2003).

[74] R. Maciuła and A. Szczurek, Phys. Rev. D **98**, 014016 (2018).

[75] E. R. Cazaroto, V. P. Goncalves, and F. S. Navarra, Phys. Rev. D **88**, 034005 (2013).

[76] D. d'Enterria and A. M. Snigirev, Phys. Rev. Lett. **118**, 122001 (2017).

[77] R. Maciuła and A. Szczurek, Phys. Lett. B **772**, 849 (2017).

[78] K. Golec-Biernat and A. M. Stasto, Phys. Lett. B **781**, 633 (2018).

[79] L. A. Harland-Lang, A. D. Martin, P. Motylinski, and R. S. Thorne, Eur. Phys. J. C **75**, 204 (2015).

[80] K. Kutak, Phys. Rev. D **91**, 034021 (2015).

[81] I. Balitsky, Nucl. Phys. **B463**, 99 (1996).

[82] Y. V. Kovchegov, Phys. Rev. D **60**, 034008 (1999).

[83] I. Balitsky and G. A. Chirilli, Phys. Rev. D **77**, 014019 (2008).

[84] J. Kwiecinski, A. D. Martin, and A. M. Stasto, Phys. Rev. D **56**, 3991 (1997).

[85] M. Bury, M. Deak, K. Kutak, and S. Sapeta, Phys. Lett. B **760**, 594 (2016).

[86] A. van Hameren, P. Kotko, K. Kutak, C. Marquet, E. Petreska, and S. Sapeta, J. High Energy Phys. 12 (2016) 034; 02 (2019) 158(E).

[87] A. van Hameren, P. Kotko, K. Kutak, and S. Sapeta, Phys. Lett. B **814**, 136078 (2021).

[88] H. Van Haevermaet, A. Van Hameren, P. Kotko, K. Kutak, and P. Van Mechelen, Eur. Phys. J. C **80**, 610 (2020).

[89] J. Alwall, R. Frederix, S. Frixione, V. Hirschi, F. Maltoni, O. Mattelaer, H. S. Shao, T. Stelzer, P. Torrielli, and M. Zaro, J. High Energy Phys. 07 (2014) 079.

[90] T. Sjostrand, S. Mrenna, and P. Z. Skands, Comput. Phys. Commun. **178**, 852 (2008).

[91] R. Gauld, U. Haisch, and B. D. Pecjak, J. High Energy Phys. 03 (2019) 166.

[92] V. P. Goncalves, B. Kopeliovich, J. Nemchik, R. Pasechnik, and I. Potashnikova, Phys. Rev. D **96**, 014010 (2017).

[93] Y. L. Dokshitzer, V. A. Khoze, and S. I. Troyan, J. Phys. **17**, 1602 (1991).

[94] S. Achatya *et al.* (ALICE Collaboration), Nature (London) **605**, 440 (2022).

[95] J. F. Gunion and G. Bertsch, Phys. Rev. D **25**, 746 (1982).